Chemical evolution of metamorphic fluids in the Central Alps, Switzerland: Insight from LA-ICPMS analysis of fluid inclusions

Journal Article

Author(s):
Rauchenstein-Martinek, Klara; Wagner, Thomas; Wälle, Markus; Heinrich, Christoph A.; Arlt, Thilo

Publication date:
2016-12

Permanent link:
https://doi.org/10.3929/ethz-b-000120718

Originally published in:
Geofluids 16(5), https://doi.org/10.1111/gfl.12194

GEOFLUIDS

Geofluids (2016) **16**, 877–908 doi: 10.1111/gfl.12194

Chemical evolution of metamorphic fluids in the Central Alps, Switzerland: insight from LA-ICPMS analysis of fluid inclusions

K. RAUCHENSTEIN-MARTINEK[1], T. WAGNER[2], M. WÄLLE[1], C. A. HEINRICH[1] AND T. ARLT[3]

[1]*Department of Earth Sciences, Institute of Geochemistry and Petrology, ETH Zurich, Zurich, Switzerland;* [2]*Division of Geology and Geochemistry, Department of Geosciences and Geography, University of Helsinki, Helsinki, Finland;* [3]*Lengnau, Switzerland*

ABSTRACT

The chemical evolution of fluids in Alpine fissure veins (open cavities with large free-standing crystals) has been studied by combination of fluid inclusion petrography, microthermometry, LA-ICPMS microanalysis, and thermodynamic modeling. The quartz vein systems cover a metamorphic cross section through the Central Alps (Switzerland), ranging from subgreenschist- to amphibolite-facies conditions. Fluid compositions change from aqueous inclusions in subgreenschist- and greenschist-facies rocks to aqueous–carbonic inclusions in amphibolite-facies rocks. The fluid composition is constant for each vein, across several fluid inclusion generations that record the growth history of the quartz crystals. Chemical solute geothermometry, fluid inclusion isochores, and constraints from fluid–mineral equilibria modeling were used to reconstruct the pressure–temperature conditions of the Alpine fissure veins and to compare them with the metamorphic path of their host rocks. The data demonstrate that fluids in the Aar massif were trapped close to the metamorphic peak whereas the fluids in the Penninic nappes record early cooling, consistent with retrograde alteration. The good agreement between the fluid–mineral equilibria modeling and observed fluid compositions and host-rock mineralogy suggests that the fluid inclusions were entrapped under rock-buffered conditions. The molar Cl/Br ratios of the fluid inclusions are below the seawater value and would require unrealistically high degrees of evaporation and subsequent dilution if they were derived from seawater. The halogen data may thus be better explained by interaction between metamorphic fluids and organic matter or graphite in metasedimentary rocks. The volatile content (CO_2, sulfur) in the fluid inclusions increases systematically as function of the metamorphic grade, suggesting that the fluids have been produced by prograde devolatilization reactions. Only the fluids in the highest grade rocks were partly modified by retrograde fluid–rock interactions, and all major element compositions reflect equilibration with the local host rocks during the earliest stages of postmetamorphic uplift.

Key words: Alps, elemental concentrations, fluid inclusions, fluid sources, halogen ratios, LA-ICPMS analysis, metamorphic fluids

Received 17 March 2016; accepted 10 August 2016

Corresponding author: Thomas Wagner, Division of Geology and Geochemistry, Department of Geosciences and Geography, University of Helsinki, P.O. Box 64 (Gustaf Hällströmin katu 2a), FI-00014 Helsinki, Finland.
Email: thomas.wagner@helsinki.fi. Tel: +358294150835.

Geofluids (2016) **16**, 877–908

INTRODUCTION

Metamorphic fluids play an important role in the structural and chemical evolution of accretionary and collisional orogenic belts (Bickle & Mckenzie 1987; Connolly & Thompson 1989; Ferry & Dipple 1991; Ferry 1994), and they are a key ingredient in hydrothermal systems that form orogenic gold deposits (Ridley 1993; Groves *et al.* 2003; Goldfarb & Groves 2015). Metamorphic fluids are derived from prograde metamorphic devolatilization processes as volatile-bearing mineral assemblages become unstable (Norris & Henley 1976; Fyfe *et al.* 1987; Oliver 1996; Phillips & Powell 2010; Tomkins 2010), and they facilitate transport of mass from deeper to shallower parts

of the crust (Bickle & Mckenzie 1987; Connolly & Thompson 1989; Ferry & Dipple 1991; Ridley 1993; Ferry 1994). Advective fluid flow during late stages of orogenic cycles (related to the exhumation and uplift) is important for the rehydration and retrogression of rocks that were previously metamorphosed at higher P-T conditions (Baumgartner & Ferry 1991; Cartwright & Buick 2000; Boiron *et al.* 2003; Yardley 2013). Fluid systems in orogenic belts may also experience deep ingression of meteoric water down to several kilometers depth, arguably even into the lower crust (Wickham & Taylor 1985; Templeton *et al.* 1999; Boiron *et al.* 2003; Menzies *et al.* 2014).

Evidences for fluid flow during regional metamorphism are quartz vein arrays in upper crustal rocks (Yardley 1983; Mullis *et al.* 1994; Cartwright & Buick 2000; Oliver & Bons 2001) and abundant fluid inclusions in metamorphic veins and their host rocks (Poty *et al.* 1974; Mullis 1975, 1987, 1988, 1996; Frey *et al.* 1980; Mullis *et al.* 1994; Agard *et al.* 2000; Touret 2001; Tarantola *et al.* 2007). Advances in microanalytical techniques such as Raman spectroscopy (Dubessy *et al.* 1989; Burke 2001; Frezzotti *et al.* 2012) and laser-ablation inductively coupled plasma mass spectrometry (LA-ICPMS) (Günther *et al.* 1997, 1998; Heinrich *et al.* 2003; Allan *et al.* 2005; Guillong & Heinrich 2007; Stoffell *et al.* 2008) now permit complete analysis of the chemical composition of individual fluid inclusions, including the volatile content and the concentrations of dissolved rock-forming elements, ore metals, sulfur and halogens (Seo *et al.* 2011). Multi-element analysis of fluid inclusions with LA-ICPMS has been widely applied to hydrothermal ore deposits (Audétat *et al.* 2000; Heijlen *et al.* 2008; Stoffell *et al.* 2008; Fusswinkel *et al.* 2013), but only few studies have addressed the composition of fluids in regionally metamorphosed terrains (Thébaud *et al.* 2006; Marsala *et al.* 2013; Miron *et al.* 2013).

This study reports the results of a fluid inclusion study of quartz fissure veins along a metamorphic cross section through the Central Alps (Switzerland). The veins are hosted by compositionally variable metamorphic rocks ranging from subgreenschist- to amphibolite-facies conditions (Fig. 1). The Central Alps are a geologically young, well-preserved orogenic belt whose geological, tectonic and metamorphic framework is well understood (Trümpy 1960; Trommsdorff 1966; Frisch 1979; Mullis *et al.* 1994; Frey & Ferreiro Mählmann 1999; Berger *et al.* 2011). The Alpine fissure veins crosscut the last peak metamorphic foliation, but show a remarkable correspondence between vein mineralogy and host-rock composition. For our study, we documented the relative time sequence of vein mineral precipitation, but essentially selected simple fissure veins showing one stage of opening and a single generation of well-developed quartz crystals directly growing from the vein wall. We avoided complex veins containing multiple quartz generations as described in Mullis *et al.* (1994), such as scepter or needle-shaped overgrowths whose stable isotope composition indicates late incursion of meteoric water (Mullis *et al.* 2001). With this sampling strategy, we can directly link the fluid inclusion results to the principal stage of vein formation and the structural framework. Our study combines fluid inclusion petrography with micothermometry and LA-ICPMS microanalysis, and we report a detailed multi-element dataset of the composition of fluid inclusion assemblages, including major rock-forming elements, ore metals, sulfur, and halogens (Cl/Br ratios). The fluid inclusion data are used to evaluate the changes in fluid composition as function of increasing metamorphic grade and to reconstruct the pressure–temperature conditions of vein formation (combining solute geothermometry with fluid inclusion isochores) relative to the peak metamorphic conditions. The analytical data are compared to the results of fluid–mineral equilibria modeling and used to constrain the processes of vein formation within the continuum between fluid- and rock-buffered environments. Finally, the concentration data for fluid–volatile elements such as halogens, boron, and sulfur are used to evaluate potential fluid sources.

REGIONAL GEOLOGICAL SETTING

Collision between the European and Adriatic continental plates resulted in long-lasting tectonic convergence in the Alpine orogenic belt (Trümpy 1960; Frisch 1979; Tricart 1984; Schmid *et al.* 1996; Handy *et al.* 2010) with several metamorphic stages recognized in different parts of the Central Alps (Fig. 1). The basement of the European margin is exposed in the external massifs, including the Aar and Gotthard massifs, which experienced a pre-Alpine history of granitoid magmatism and high-grade metamorphism during several Paleozoic orogeneses. The southern Alps represent the Adriatic microplate, parts of which were overthrust as Austroalpine Nappes over much of the Penninic domain and the southern margin of the European continent (Hurford 1986; Hunziker *et al.* 1989; Vialon 1990; Hsü 1991; Mullis *et al.* 1994; Schmid *et al.* 1996; Pfiffner *et al.* 2000; Wiederkehr *et al.* 2009). The Penninic domain consists of a complex nappe stack of continental basement slices, former oceanic crust (ophiolites), and accrectionary wedge metasediments (Bündnerschiefer). Some units of the Penninic nappe stack experienced Eocene to Early Oligocene subduction metamorphism ranging from blueschist to eclogite facies (notably the Adula Nappe between Vals and Locarno; Heinrich 1986; Oberhänsli *et al.* 1995), prior to the establishment of the consistently north-vergent nappe stack (Schmid *et al.* 1996; Pfiffner *et al.* 2000; Wiederkehr *et al.* 2009). Collision and crustal thickening led to Barrovian-style regional

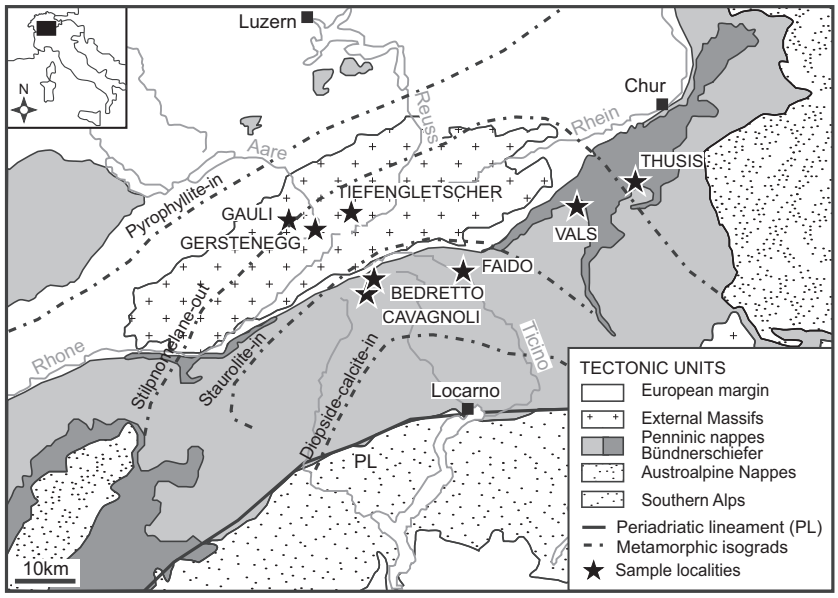

Fig. 1. Map of the Central Alps showing essential geological features (major tectonostratigraphic units, metamorphic isograds) and the location of the sampled Alpine fissure veins. The collisional nappe complexes of the Penninic domain (gray shading) are located between the European continent (white) and the partly overthrusted African or Adriatic plate (stippled). Dashed–dotted lines indicate the main mineral isograds (pyrophyllite-in, stilpnomelane-out, staurolite-in, and diopside calcite-in). Adopted from Frey & Ferreiro Mählmann (1999). Redrawn and modified from Rauchenstein-Martinek *et al.* (2014).

metamorphism of Oligocene to Miocene age, whose isograds cross all nappe boundaries and are domed up in the asymmetric Lepontine metamorphic dome (Fig. 1; Niggli & Niggli 1965; Trommsdorff 1966; Niggli 1970; Wenk 1970; Frey *et al.* 1980; Todd & Engi 1997; Bousquet *et al.* 1998; Frey & Ferreiro Mählmann 1999; Wiederkehr *et al.* 2009). Upper amphibolite-facies units with partial anatexis were exhumed along its southern flank and highest temperature isograds are truncated by the Insubric Line as part of the Periadriatic Lineament south of Locarno (Berger *et al.* 2009; Rubatto *et al.* 2009), whereas peak metamorphic grade decreases more gradually northward through the external massifs as a result of the asymmetric uplift of the metamorphic dome during Miocene times (Schlunegger & Willett 1999; Janots *et al.* 2009; Berger *et al.* 2011).

The Alpine fissure veins formed when their metamorphic host rocks were exhumed and crossed the ductile–brittle transition. This resulted in the opening of fractures, and fluids from the local host rock or from deeper parts of the crust were drained into the veins (Burkhard & Kerrich 1988; Marquer & Burkhard 1992; Mullis *et al.* 1994; Mullis 1996; Tarantola *et al.* 2007, 2009). The age of the Alpine fissure veins is constrained by geochronological data that include older K-Ar dates of adularia and white mica (Purdy & Stalder 1973) and more recent U-Pb and U-Th-Pb ages of accessory minerals (Sharp *et al.* 2005; Janots *et al.* 2012). The K-Ar dates point to vein formation during the broad time interval between 16 and 9 Ma in the Aar and Gotthard massifs in the Central Alps (Purdy & Stalder 1973), but are subject to uncertain degrees of resetting and/or excess argon. U-Pb dating of titanite from the Gotthard massif yielded an age of 15.2 Ma (Sharp *et al.* 2005), and recent U-Th-Pb dating of monazite demonstrated two distinct times of 15.5–14.7 Ma and 13.8–13.6 Ma (Janots *et al.* 2012), but both are paragenetically late mineral growths relative to the large quartz crystals studied here.

The Alpine fissure veins sampled for this study (Fig. 1, Table 1) are located on a metamorphic cross section through the Lepontine dome of the Central Alps, from the Aar massif in greenschist-facies overprinted basement rocks to the Penninic nappes in amphibolite-facies gneisses and metasedimentary rocks. The central part of the Lepontine dome experienced amphibolite-facies metamorphism at about 35–30 Ma (Trommsdorff 1966; Grujic & Mancktelow 1996). The core set of sampled fissure veins are hosted by similar quartz–feldspar–mica-bearing lithologies (metagranites or semipelitic schists and gneisses; Table 1), including Gauli (chlorite–mica schist), Gerstenegg (metagranodiorite), Tiefengletscher (metagranite), Cavagnoli (mica schist), and Faido muscovite–biotite gneiss) (Fig. 1). The Gerstenegg fissure vein is exposed in an underground tunnel of the Grimsel power plant and is a protected geoheritage site (Stalder 1986). The core sample suite was complemented by additional fissure veins that are exposed in more diverse host rock lithologies, including Thusis (carbonaceous calc schist), Vals (mafic mica schist), and Bedretto (calc schist).

GEOLOGY AND MINERALOGY OF SAMPLING LOCALITIES

The Alpine fissure veins are late-tectonic mineral veins that are not completely filled, but they contain open fissures and cavities in their central part that host euhedral crystal

Table 1 Summary description of the investigated metamorphic vein systems, Central Alps.

Locality	Altitude	Tectonostratigraphic unit	Host-rock mineralogy	Vein assemblage	Fluid inclusions	Th of fluid inclusions	Fluid X_{CO_2}	Vein temperature–pressure conditions	Peak metamorphic conditions
Thusis	1640 m	North Penninic Nappes Bündnerschiefer	Chlorite, illite, albite, quartz, calcite	Quartz + chlorite → calcite → cookeite	Type: H_2O-NaCl Salinity: 4.0 wt.%	130 ± 2°C	<0.03	T: 290–320°C P: 2.8–3.8 kbar	T: 300–340°C P: 2.8–3.8 kbar
Vals	1500 m	North Penninic Nappes Tomül ophiolite	Quartz, biotite, amphibole, muscovite, plagioclase	Quartz + epidote → chlorite → minor calcite	Type: H_2O-NaCl Salinity: 2.9 wt.%	180 ± 10°C	0	T: 300–350°C P: 2.8–3.8 kbar	T: 450–500°C P: 5.0–7.0 kbar
Gauli	2400 m	Aar massif Northern schist zone	Plagioclase, K-feldspar, quartz, muscovite, chlorite, biotite, epidote	Quartz + adularia + epidote → titanite → chlorite	Type: H_2O-NaCl Salinity: 4.7 wt.%	151 ± 6°C	0	T: 320–380°C P: 2.8–4.6 kbar	T: 430–470°C P: 3.9–5.9 kbar
Gerstenegg	2100 m	Aar massif Grimsel granodiorite	Quartz, K-feldspar, plagioclase, biotite	Quartz + adularia → calcite → fluorite → chlorite	Type: H_2O-NaCl Salinity: 10.2 wt.%	185 ± 3°C	0	T: 330–350°C P: 2.2–3.2 kbar	T: 420–460°C P: 2.9–4.7 kbar
Tiefengletscher	2800 m	Aar massif Central Aar granite	Quartz, K-feldspar, plagioclase, chlorite, biotite	Quartz → chlorite	Type: H_2O-NaCl Salinity: 9.3 wt.%	210 ± 7°C	0	T: 350–430°C P: 2.1–3.9 kbar	T: 420–480°C P: 3.2–4.8 kbar
Bedretto	2500 m	Penninic cover Bündnerschiefer	Quartz, muscovite, calcite, biotite	Quartz + adularia → muscovite → calcite + rutile	Type: H_2O-CO_2-NaCl Salinity: 0.4 wt.%	285 ± 10°C	0.14	T: 300–340°C P: 1.5–2.8 kbar	T: 460–530°C P:5.0–6.7 kbar
Cavagnoli	2640 m	Penninic nappes Lebendun gneiss	Quartz, muscovite, biotite	Quartz + adularia → muscovite	Type: H_2O-CO_2-NaCl Salinity: 0.4 wt.%	295 ± 8°C	0.13	T: 300–350°C P: 1.4–2.9 kbar	T:460–530°C P: 5.0–6.7 kbar
Faido	710 m	Penninic nappes Lucomagno gneiss	Quartz, biotite, plagioclase, K-feldspar, muscovite	Quartz + albite + muscovite → ankerite	Type: H_2O-CO_2-NaCl Salinity: 3.4 wt.%	299 ± 12°C	0.13	T: 300–340°C P: 1.5–2.8 kbar	T: 530–600°C P: 5.5–7.0 kbar

assemblages. The vein mineral assemblages closely reflect the host rock composition, with significant mineralogical differences between metapelites, metagranites, and metabasic rocks (Stalder *et al.* 1973; Mullis 1975, 1987, 1988; Mullis *et al.* 1994). Metasomatic alteration zones surrounding the veins are of limited extent, usually comparable to vein volume or smaller, and characterized by depletion in components that are found as major vein filling (note that the terms alteration and metasomatism are used interchangeably in this paper; Yardley 2013). The veins can reach sizes from few centimeters to several meters in thickness and commonly have characteristic sigmoidal shapes (Fig. 2). In the Aar and Gotthard massifs, the Alpine fissure veins are oriented more or less horizontally, crosscutting the steep local foliation dominated by pre-Alpine metamorphism, whereas in the Penninic nappes, they are mostly subvertical (Demartin *et al.* 1994; Hofmann & Knill 1996; Frey & Ferreiro Mählmann 1999; Weisenberger & Bucher 2010). Regardless of the structural style and host-rock lithologies, all fissure veins have characteristic textural features, which include a narrow (centimeter- to decimeter-sized) alteration selvage adjacent to the vein wall-rock contact grading into fresh wall rock, a zone of anhedral, massive quartz grown onto the vein wall-rock contact, and euhedral crystal assemblages, which overgrow the massive quartz. The massive quartz may completely fill the fissure veins at their terminations. Frequently, fine-grained vermicular chlorite has precipitated on top of the euhedral crystals.

Thusis

The samples come from a 1-by-3-m-sized fissure vein above Thusis, which has already been described and

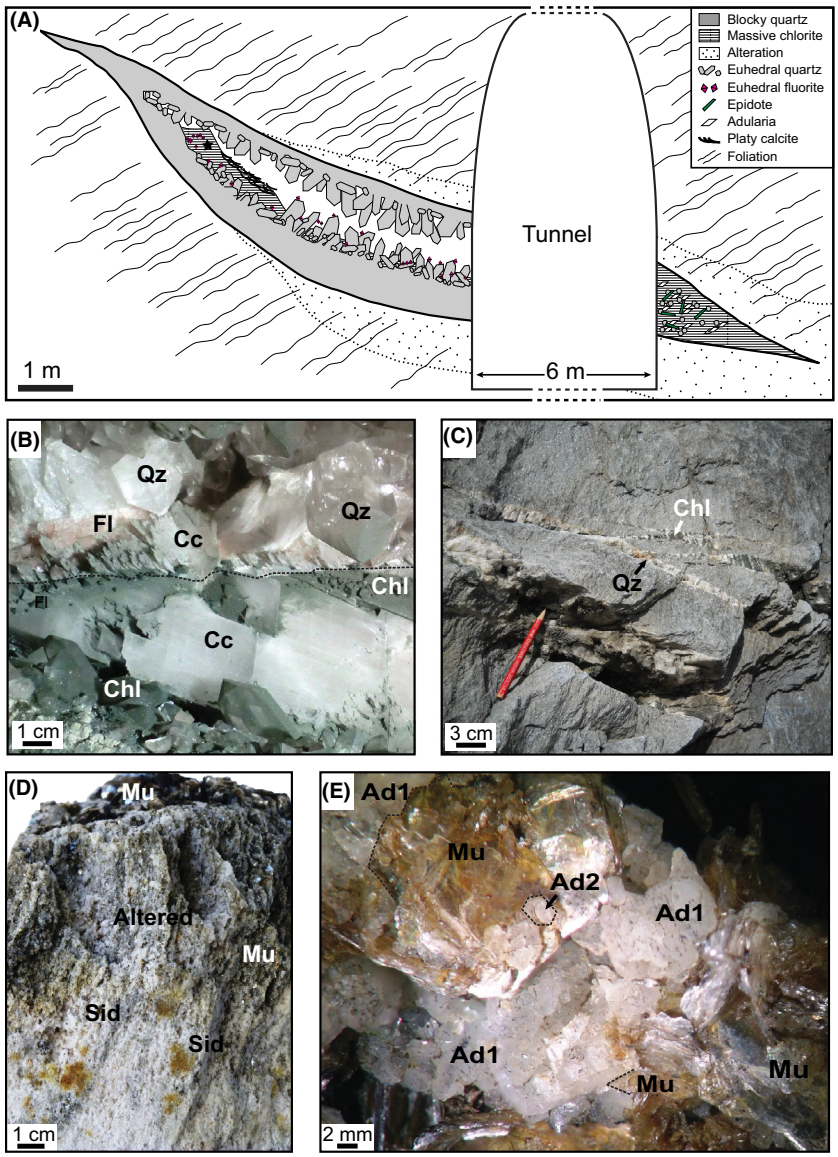

Fig. 2. Field and hand-specimen relationships of Alpine fissure veins. (A) Simplified cross section through the Gerstenegg fissure vein. The upper termination of the vein is filled with massive quartz, whereas the lower termination contains mostly vermicular chlorite, epidote, and adularia. The euhedral quartz crystals are mostly located in the central part of the vein. The upper part of the vein hosts one large calcite crystal overgrown by a late generation of bladed calcite. (B) Close-up view of the large calcite crystal of the Gerstenegg vein. Note that all minerals below the stippled line are covered with fine-grained vermicular chlorite, whereas minerals above the line are not chlorite covered. The late-stage bladed calcite crystals emerge from the stippled line, interpreted as an internal liquid—vapor 'water table' at a late stage in the mineralogical evolution of the vein. (C) Set of flat-lying quartz-chlorite veinlets with one larger fissure vein (bottom) hosting euhedral crystal assemblages; Gauli. (D) Alteration halo of muscovite + albite + adularia + siderite surrounding fissure vein hosted in muscovite-biotite gneiss, showing porous structure from which all quartz was leached out; Faido. The vein contains euhedral quartz and muscovite crystals. (E) Fissure vein assemblage composed of quartz, muscovite, and two generations of adularia (Ad1 and Ad2); Bedretto. Muscovite has formed largely coeval with the younger adularia generation. Mineral abbreviations: Qz, quartz; Chl, chlorite; Cc, calcite; Fl, fluorite; Mu, muscovite; Sid, siderite; Ad, adularia.

analyzed by Miron *et al.* (2013). The metapelitic Bündnerschiefer host rocks are rich in carbonates, organic matter, and quartz. The vein minerals are elongated and comprise blocky quartz crystals overgrowing pale green chlorite, and calcite with minor cookeite in the center of the open cavity.

Vals

The Vals fissure vein samples are situated in the Tomül nappes of the Misox ophiolite zone. The host rocks are mafic schists composed of actinolite, clinozoisite, albite, minor quartz, chlorite, and accessory titanite. The amphiboles are often replaced by chlorite at their rims. The few mm-thick alteration zone surrounding the fissure veins is only visible around the lower part of the veins and is characterized by an increase in chlorite and minor actinolite and tremolite. Within the open cavities of the more horizontally oriented vein, euhedral quartz crystals, epidote, chlorite and calcite are present. The quartz crystals growing on the footwall of the fissure vein are covered by fine-grained chlorite, and they also contain chlorite inclusions, whereas the quartz grown on the hanging wall is chlorite free. The carbonate minerals only appear as a late phase on the chlorite covered quartz crystals.

Gauli

The host rocks of the fissure veins in the Gauli region are composed of quartz, plagioclase, K-feldspar, muscovite, calcite, biotite, chlorite, and the accessory minerals titanite and apatite. The large porphyroclasts of quartz, K-feldspar, and plagioclase are deformed and elongated parallel to the foliation, which is defined by biotite that is partly retrograded to chlorite and muscovite. This structure suggests that the host rocks are likely metamorphosed arkosic sedimentary rocks. Fissure veins in the Gauli region include abundant quartz–chlorite veinlets, whereas larger open fissure veins with euhedral crystal assemblages are found in a narrow zone close to the Gauli glacier. The larger open fissure veins are typically associated with several smaller veinlets mostly filled with massive quartz. Together, they form sets of veins that are arranged en echelon. The studied samples come from two parallel open fissure veins located just next to the current margin of the Gauli glacier (about 3 m distance from each other). They are up to 1 m in thickness and 3–5 m in length. The veins are surrounded by a 2- to 3-cm-thick leaching zone composed of feldspars and muscovite and minor quartz and chlorite. The vein wall is covered with blocky quartz, which is overgrown by euhedral open space-filling minerals. Albite crystals are overgrown by quartz and adularia, followed by a chlorite cover in the lower part of the fissure vein. In this part, the chlorite covered quartz crystals contain also cm-sized titanite and minor epidote crystals on top.

Gerstenegg

The Gerstenegg fissure vein is situated in the Grimsel granodiorite that is mainly composed of plagioclase, K-feldspar, amphibole, biotite, muscovite, and chlorite. In the vicinity of the fissure vein, the biotite is altered to muscovite and chlorite and the feldspars are partly replaced by sericite. The main Gerstenegg fissure vein is about 9 m long and 5.6 m thick and preserved as a publicly accessible, protected geological site inside the KWO power plant (Stalder 1986). It is part of a set of essentially parallel fissure veins, which crosscut the main foliation of the metagranodiorite host rock at high angles. Our samples come from the middle part and the lower and upper terminations of the main fissure vein (Fig. 2A). The vein is surrounded by an alteration selvage of several centimeters thickness that is well developed in the central and lower part of the vein, but largely absent in the upper part. The alteration close to the lower termination of the vein (where the vein is filled by chlorite, adularia, and epidote) is manifested by a porous and bleached host rock that clearly has lost most of its quartz without obliteration of the metagranitoid texture.

The upper termination of the fissure vein is filled with massive quartz, which continuously grades into the open cavity as euhedral quartz crystals in places where the vein is thicker than about 30 cm. The most abundant mineral in the open fissure is quartz which is present as euhedral crystals with sizes of few cm up to 20 cm. A large blocky calcite crystal is present close to the upper termination of the vein. This blocky calcite shows a prominent subhorizontal line along the surface (Fig. 2B). From this line, a younger generation of platy calcite crystals emerges and the part below the line is covered by vermicular chlorite, whereas the part above the line does not have a chlorite overgrowth. This chlorite also grows on top of abundant pink fluorite crystals of 0.5–1.0 cm size that have grown on top of the quartz and the calcite. The center of the Gerstenegg vein contains an accumulation of sandy chlorite with some platy calcite crystals (Fig. 2A). Sandy chlorite, apparently sedimented in the cavity as late-precipitating mineral, also occurs in the lower part of the fissure near the visitor window in the main tunnel (Fig. 2A). This chlorite completely fills the lowest tip of the vein on the other side of the tunnel, where none of the other minerals occur. The sulfide minerals pyrite and galena are present in trace amounts in the middle part of the fissure vein in a narrow vein that branches off from the main vein (Stalder 1986). In the lower part of the fissure vein that is surrounded by an extensive alteration and leaching halo, the rock-forming minerals of the Grimsel granodiorite epidote, titanite, and apatite have crystallized inside the vein, together with

abundant adularia crystals. Fluorite, galena, and milarite were exclusively found inside the cavity (Stalder 1964, 1986; Mercolli *et al.* 1984).

Tiefengletscher

In the proximity of the Tiefengletscher, Peter Indergand Sr. discovered a quartz crystal group in 1946, which represents one of the most spectacular groups of smoky quartz ever found in the Alps and is now hosted by the focus-Terra museum at ETH Zurich. Our studied quartz samples originate from the same fissure as the Indergand specimen. The host rock is the central Aar granite, which is composed of plagioclase, K-feldspar, biotite, muscovite, and chlorite. The fissure vein belongs to a set of several parallel veins that are oriented horizontally and crosscut the host-rock foliation at a high angle. The vein is about 8 m in length and opens up in the center to an open cavity of 70 to 120 cm in width. The dark smoky quartz crystals reach sizes up to 45 cm and are associated with calcite, chlorite, and apatite (Indergand-Helfenstein 2005).

Bedretto

The fissure veins in the Bedretto valley are hosted by Bündnerschiefer metasedimentary rocks of amphibolite-facies metamorphic grade (Wiederkehr *et al.* 2009). They are composed of dominantly quartz, muscovite, carbonates, amphibole, and altered biotite, with staurolite, garnet, and biotite in metapelitic rocks nearby. The samples originate from a set of almost vertical, typically cm-wide fissure veins. The investigated area contains a large number of individual veins, but only few of them are thicker than 10 cm and host open cavities. They are bordered by a selvage of altered host rocks, and both the alteration zones and the veins contain relicts of carbonate minerals that are largely weathered. The vein mineral assemblage comprises quartz and muscovite, and minor amounts of calcite, adularia, and rutile. Following a thin marginal zone of anhedral quartz that is directly grown onto the wall rock, euhedral crystals form the central part of the vein filling. The euhedral quartz is intergrown with adularia and muscovite crystals and the textural relationships suggest essentially synchronous growth of all three minerals (Fig. 2E). Adularia is present as two distinct generations, with earlier large white adularia crystals overgrown by later smaller crystals of brownish adularia. Sometimes, the lower parts of the veins are completely filled by up to 10-cm-sized adularia crystals, while the upper parts contain mostly quartz.

Cavagnoli

The fissure veins in the Cavagnoli area are hosted by gneisses that have a metasedimentary protolith. They consist of plagioclase, angular quartz, K-feldspar (partly altered to sericite), green hornblende, biotite, muscovite, and titanite. The fissure veins have a subvertical orientation and occur in a structural corridor that extends from the Bedretto valley to the higher mountains south of the Cavagnoli valley. The veins have typical thicknesses of few cm and most veins are completely filled by quartz. Few veins are up to 50 cm thick and contain open cavities with euhedral crystals. The mineral assemblage is similar to Bedretto, with an intergrowth of quartz, adularia and muscovite making up most of the vein filling. In addition, rutile crystals have locally grown on top of euhedral quartz crystals.

Faido

The samples come from a set of fissure veins exposed in an underground exploration tunnel built for the NEAT railway tunnel in the Lucomagno gneiss. The unaltered host-rock gneiss is composed of quartz, biotite, plagioclase, K-feldspar, muscovite, and ankerite. The alteration and leaching zone surrounding the fissure veins contains mainly K-feldspar and plagioclase and only minor quartz. Because the veins are exposed several hundred meters below the surface, the full mineral assemblage including the carbonate phases is preserved. The veins are subvertically oriented and their structure resembles those of the Bedretto and Cavagnoli area. The upper part of the fissure veins is commonly completely filled by massive quartz that is overgrown by euhedral quartz crystals in the central open cavity. The lower part of the veins typically contains larger proportions of muscovite and adularia associated with quartz crystals, and the crystal faces of all three minerals are sometimes covered by vermicular chlorite. Rarely, small crystals of ankerite and calcite have grown on top of quartz crystals and the chlorite. Only the central part of the fissure vein contains abundant muscovite that is associated with quartz and adularia.

ANALYTICAL METHODS

Whole-rock geochemistry

Whole-rock samples (including hydrothermally altered wall rocks of fissure veins and fresh host rocks sampled at few meters distance from the veins) were analyzed for the concentrations of major and minor elements, inorganic and organic carbon, sulfur, and ferrous and total iron. Major and minor element concentrations were determined by wavelength-dispersive X-ray fluorescence spectroscopy (XRF) with a PANalytical Axios instrument, using glass beads prepared from dry rock powder and lithium tetraborate. The FeO content was determined at the University of Lausanne by wet chemistry and colorimetric methods (Wilson 1960; Johnson & Maxwell 1981; Wülser *et al.* 2011).

The carbon content was determined with a UIC Inc. CM 5012 carbon analyzer. The carbon in the sample is combusted in a furnace (CM 5200) and then introduced into the coulometer, and this analysis yields the total carbon content. The inorganic carbon content (i.e., carbon dioxide) is determined separately by acid digestion (CM 5130). The organic carbon content is then calculated as the difference between total and inorganic carbon. The water content was not directly determined, but calculated from the loss on ignition, the carbon and sulfur content, and the ferrous/ferric iron ratio.

Fluid inclusion microthermometry

Fluid inclusion assemblages (FIA), that is groups of fluid inclusions that were trapped coevally on constrained growth zones or healed fractures (Goldstein & Reynolds 1994; Touret 2001), were established by detailed fluid inclusion petrography. All fluid inclusion data are reported as assemblage averages with their standard deviations. Fluid inclusion microthermometry was performed using a Linkam THMSG-600 freezing–heating stage, attached to a Leitz optical microscope. The calibration was performed on synthetic fluid inclusions of pure H_2O (final ice-melting temperature: 0.0°C, homogenization temperature: 374.0°) and CO_2 (final CO_2 ice-melting temperature: −56.6°C) from SYNFLINC. The aqueous two-phase inclusions were cooled to −100°C, then heated at a rate of 100°C min^{-1} to −20°C, heated with 10°C min^{-1} until −10°C, and then with 1°C min^{-1} and 0.5°C min^{-1} close to the final ice-melting temperature (Tm_{ice}). Total homogenization temperatures (Th_{tot}) were measured by heating the fluid inclusions at a rate of 100°C min^{-1} up to 150°C and then with 1°C min^{-1} close to the homogenization temperature. The aqueous–carbonic three-phase inclusions were cooled to −100°C and then heated with 20°C min^{-1} to −60°C and 1°C min^{-1} close to the final CO_2 ice-melting temperature (Tm_{CO_2}). Subsequently, the fluid inclusions were heated at a rate of 50°C min^{-1} to −10°C and with 0.5°C min^{-1} close to the clathrate melting temperature (Tm_{Cla}). Partial homogenization temperatures of the CO_2 phase (Th_{CO_2}) were determined by warming the fluid inclusions from room temperature with 5°C min^{-1} and then with 1°C min^{-1} close to the homogenization temperature. Total homogenization temperatures were only determined for some inclusions from a given FIA and were typically measured after the elemental composition of larger fluid inclusions had been analyzed by LA-ICPMS. Total homogenization was measured by heating the fluid inclusions with 50°C min^{-1} to 200 or 250°C and then with 2°C min^{-1} close to the homogenization temperature. The precision of the microthermometric measurements is about ±0.1°C for melting temperatures and ±1°C for homogenization temperatures, based on replicate measurements of the calibration standards.

Salinities were calculated as wt.% equivalent (eqv.) NaCl from the final ice-melting temperature for the aqueous inclusions (Bodnar 1993) and from the CO_2 clathrate melting temperature for the aqueous–carbonic inclusions (Diamond 1992). Fluid inclusion densities and isochores were calculated with the FLUIDS software package (Bakker 2003). For aqueous fluid inclusions, the bulk density was calculated from the microthermometric data alone, using the equation for H_2O-NaCl of Zhang & Frantz (1987) as implemented in the FLUIDS program of Bakker (2003). For aqueous–carbonic inclusions, the volume proportions of the CO_2 and H_2O phases had to be estimated. This was performed by heating the inclusions to 40°C, where both the aqueous and carbonic phases are assumed to be close to the pure end-member composition, the H_2O phase is nearly incompressible and the pressure is fixed by the isochore for the one-phase CO_2 fluid at 40°C (Burrus 1981). The area fractions of the CO_2 and H_2O phases were then estimated graphically, and area fractions were extrapolated to volume fractions to obtain the bulk $CO_2/(CO_2 + H_2O)$ ratio.

LA-ICPMS microanalysis of fluid inclusions

Individual fluid inclusions were analyzed using the ETH-GeoLas system (193 nm excimer laser) connected to an ICP-quadrupole-MS (Perkin Elmer Elan 6100 DRC) (Günther *et al.* 1997; Heinrich *et al.* 2003). To increase the sensitivity for heavier trace elements, H_2 was added to the Ar flow with 5 ml min^{-1} (Guillong & Heinrich 2007). For controlled complete ablation of the quartz-hosted fluid inclusions, an energy density above 15 J cm^{-2} and a laser pulse frequency of 10 Hz was used. The optical imaging system permits a rapid widening of the ablation crater from 10 to 120 μm at constant laser energy density by adjusting an aperture in the laser beam path. In the fluid inclusions, the following elements were analyzed: Li, Na, K, Rb, Cs, Mg, Ca, Sr, Ba, B, Al, Fe, Mn, Cu, Zn, Pb, Ag, As, Sb, Ti, S, Cl, and Br. Selected fluid inclusions from the FIA that were analyzed with this multi-element menu were also measured with a reduced menu optimized for analyzing the Cl/Br ratio (Seo *et al.* 2011). This element menu included only Na, Rb, Cl, and Br. The Ca concentration was measured on isotope ^{44}Ca, which has about three times higher isotopic abundance than ^{42}Ca. Although ^{44}Ca is affected by interference from $^{28}Si^{16}O^{+}$ produced from ablation of the host quartz, the effect is small and can be corrected for by host background subtraction. NIST-610 was used as standard material for most of the elements except Cl and Br where the Sca-17 scapolite standard (Seo *et al.* 2011) was applied. Element concentrations were quantified using the SILLS software package that

deconvolves the host mineral and fluid inclusion signal (Guillong *et al.* 2008). The analyzed element ratios were converted into absolute concentrations using the microthermometrically determined salinity. Because most fluid inclusions contain considerable concentrations of K and Ca, the common salt correction procedure was used (Heinrich *et al.* 1992).

Each fluid inclusion signal was screened and only data with clearly visible peaks and intensities above 3σ of the background were considered for calculation of element concentrations (Fig. 3). In addition, signals were screened for the presence of accidentally trapped solid phases inside the fluid inclusion, which are typically associated with a large simultaneous increase in a group of elements compared to the fluid inclusion assemblage average (about half to one order of magnitude). The detection limit for each element varied as a function of the size of the fluid inclusions, and some elements could therefore only be quantified in larger inclusions. Some inclusions were analyzed for a smaller subset of elements focused on ore metals and are included here, but were published separately in Rauchenstein-Martinek *et al.* (2014).

Phase equilibria computation

Fluid–mineral equilibria modeling in the multicomponent multiphase system Na-K-Ca-Mg-Fe-Si-Al-C-S-H-O-Cl was performed with the GEMS3 Gibbs free energy minimization package (Karpov *et al.* 1997; Wagner *et al.* 2012; Kulik *et al.* 2013). The calculations account for fluid speciation, mineral solubility, and solid solution effects of the main rock-forming minerals and predict fluid composition, pH, and oxidation state as function of pressure and temperature and bulk rock composition. The thermodynamic dataset employed was based on the model used earlier (Dolejs & Wagner 2008), with additions for aqueous carbon and sulfur species, carbonate and sulfide minerals, and their solid solutions. Data for aqueous species came from the SUPCRT92 dataset and updates (Shock & Helgeson 1988; Shock *et al.* 1989, 1997; Johnson *et al.* 1992; Sverjensky *et al.* 1997; Tagirov *et al.* 1997; Tagirov & Schott 2001), while data for rock-forming minerals came from the Holland–Powell internally consistent dataset (Holland & Powell 1998; Evans *et al.* 2010). The activity–composition relationships for rock-forming mineral solid solutions were modeled by ideal, nonideal, symmetric, and asymmetric models (Powell & Holland 1993, 1999; Holland & Powell 1996, 1998, 2003; Holland *et al.* 1998; Coggon & Holland 2002; Wei *et al.* 2003; Dale *et al.* 2005; Evans *et al.* 2010). Activity coefficients of aqueous species and water solvent were calculated from an extended Debye-Hückel model (Helgeson *et al.* 1981; Walther 1997, 2001). The overall uncertainty of the phase equilibria computation is largely determined by the uncertainty of the thermodynamic data and is estimated as approximately 0.5 log units in the predicted equilibrium

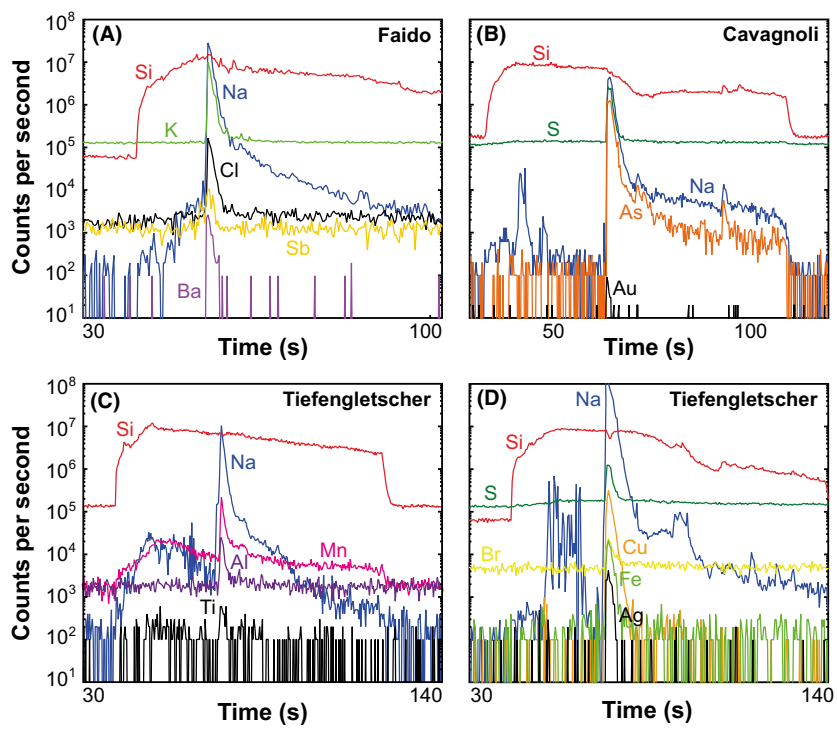

Fig. 3. Representative LA-ICPMS signals for aqueous–carbonic (A, B) and aqueous (C, D) fluid inclusions. The sharp increase in Si above background indicates the onset of quartz host ablation and the large Na peak the breaching of the fluid inclusion. The signals for all elements analyzed (of which only K, Ba, Fe, Mn, Cu, Ag, Au, As, Sb, Al, Ti, and/or Cl are shown) closely follow the shape of the Na signal, reflecting the absence of any daughter or accidentally trapped solids.

concentrations of dominant aqueous species (Johnson *et al.* 1992; Sverjensky *et al.* 1997).

Fluid–mineral equilibria were computed for five Alpine fissure vein systems that cover localities from greenschist to amphibolite facies and different host-rock lithologies (metagranite, gneiss, mica schist, and mafic greenschist). The calculations were run over a large range of temperatures from 200 to 600°C and at the estimated vein-forming pressure of 3.0, 2.5, 3.0, 2.0, and 1.8 kbar for the localities Tiefengletscher, Gerstenegg, Gauli, Faido, and Cavagnoli, respectively. The analyzed whole-rock composition was converted into the model system SiO_2-Al_2O_3-Fe_2O_3-FeO-MgO-CaO-Na_2O-K_2O-CO_2-S-H_2O (Table 2). This simplification was performed by subtracting TiO_2 and stoichiometric amounts of CaO proportional to the amount of P_2O_5, accounting for modal rutile and apatite. The recalculated whole-rock composition was then normalized to 1000 g. The input fluid was based on the observed fluid inclusion composition of each locality, but initially simplified to the major salt and volatile components H_2O-CO_2-H_2S-NaCl (Table 3). Fluid–rock equilibria were calculated at rock-dominated conditions, using a fixed mass-based input fluid/rock ratio of 0.1, to predict the concentrations of all aqueous species as well as the composition and abundance of minerals at equilibrium. Due to mineral dissolution and precipitation that change as function of temperature and pressure, the calculated output equilibrium fluid/rock ratios vary slightly from the initial input fluid/rock ratio.

FLUID INCLUSION RESULTS

Inclusion petrography

Fluid inclusion studies focused on euhedral quartz crystals of 3 to 10 cm in size. The quartz crystals contain several sequential growth zones, which constrain the relative chronology of different fluid inclusion assemblages in relation to the crystal growth (Figs 4 and 5). The fluid inclusions are typically 10–250 μm in size in all investigated samples. We selected fluid inclusion assemblages that contained a sufficient number of inclusions of 50–120 μm in size for detailed microthermometry and LA-ICPMS analysis, permitting multi-element LA-ICPMS analysis with good sensitivity and reproducibility for each FIA.

In the Gauli samples, the oldest FIA were found in the anhedral marginal zone of the quartz that lines the vein wall. These fluid inclusions (FI) have typically sizes of 20 to 60 μm. They occur as numerous pseudosecondary trails, which terminate at grain boundaries (Fig. 4, Type 1; corresponding to assemblages A1 to A7 in Table 4 and Data S1). This zone is overgrown by euhedral quartz crystals. They contain numerous pseudosecondary fluid inclusions within their core, adjacent to the anhedral quartz at the base of the crystals. Most of the FI in this part of the crystal are aligned on pseudosecondary trails, whereas few larger FI (up to 200 μm) with irregular shape occur as groups without a clear relation to healed microfractures or growth zones. The fluid inclusion-rich cores of the quartz crystals are overgrown by a highly transparent quartz, which is typically separated from the core by a euhedral growth zone (Type 4 in Fig. 4; corresponding to FIA A8 to A14 in Table 4 and Data S1). This outer part of the quartz crystals contains mainly trails of secondary FI, which also crosscut the older cores of the crystals. All fluid inclusions in the Gauli samples are aqueous two-phase (LV) inclusions with similar phase proportions.

The samples from Gerstenegg, Tiefengletscher and Vals contain fluid inclusion assemblages with a chronology that is similar to that of the Gauli samples. The crystals contain mainly pseudosecondary FI in an inclusion-rich core and clearer outer growth zones (one or sometimes several ones) that mainly contain secondary FI (Fig. 5). The secondary FI are aligned on well-defined long trails that crosscut the older trails with pseudosecondary FI in the core of the crystals. In the Gerstenegg samples, euhedral fluorite crystals that have grown on top of the quartz crystals contain distinctly later fluid inclusions with smaller bubbles. All fluid inclusions from Gerstenegg, Tiefengletscher, and Vals are aqueous two-phase (LV) inclusions.

The quartz crystals in the samples from Bedretto, Cavagnoli and Faido contain a core with abundant FI aligned on many short pseudosecondary trails (Fig. 6). The crystal cores are overgrown by one or several clearer growth zones that contain few short trails with pseudosecondary FI, but otherwise, the crystals host mainly secondary FI on distinct trails that also crosscut the rim and core of the crystals. The relative timing of the pseudosecondary FI in the clearer outer parts of the crystals is difficult to establish. They are younger than the pseudosecondary FI in the crystal cores, but may be older or have the same relative age as the secondary FIA that are aligned on the larger crosscutting trails. All fluid inclusions in the samples from Bedretto, Cavagnoli and Faido are aqueous–carbonic three-phase (LLV) inclusions with apparently identical phase proportions.

Microthermometry

Consistent with previous regional studies (Mullis *et al.* 1994), the Alpine fissure veins of this study contain two-phase aqueous fluid inclusions of the LV-type in greenschist-facies rocks in the northern part of the study area (Thusis, Vals, Gauli, Gerstengg and Tiefengletscher)

Table 2 Summary of whole-rock geochemical data, including major and minor elements and volatiles (inorganic and organic carbon, sulfur). Analytical totals were calculated from major element oxides (total iron expressed as ferric iron) and loss on ignition (LOI).

Sample	ICM-G-2 Gauli	ICM-G-3 Gauli	ICM-G-9 Gauli	ICM-GE-2 Gerstenegg	ICM-GE-3 Gerstenegg	ICM-GE-4 Gerstenegg	ICM-GE-5 Gerstenegg	ICM-GE-6 Gerstenegg	ICM-C-1 Cavagnoli	ICM-F-2 Faido
Wt.%										
SiO_2	68.76	67.19	64.88	66.73	69.13	68.50	68.57	66.70	60.44	70.95
TiO_2	0.45	0.66	1.37	0.66	0.63	0.57	0.70	0.59	0.66	0.38
Al_2O_3	15.80	15.65	17.82	16.97	15.99	16.75	15.97	16.83	21.17	13.73
Fe_2O_3	1.12	1.35	0.92	0.95		1.08	1.46		2.71	1.63
FeO	1.78	2.70	0.46	0.07		0.34	0.57		0.21	0.80
MnO	0.04	0.05	0.02	0.02	0.02	0.03	0.04	0.06	0.02	0.04
MgO	0.96	1.34	0.46	0.15	0.21	0.28	0.48	0.76	0.62	0.38
CaO	1.85	1.84	2.86	2.36	2.46	2.55	2.92	2.77	0.43	1.34
Na_2O	3.22	3.56	5.02	6.23	5.46	5.23	4.85	5.02	4.12	4.28
K_2O	4.12	3.86	4.25	3.46	3.33	4.03	3.56	3.56	7.78	4.56
P_2O_5	0.22	0.27	0.47	0.19	0.19	0.18	0.23	0.19	0.15	0.19
CO_2	1.31	2.16	0.03	0.25	0.07	0.13	0.26	0.22	0.09	0.71
C (org)	0.10	0.37	0.26	0.00	0.03	0.00	0.02	0.01	0.27	0.01
S	0.00	0.03	0.00	0.00	0.00	0.00	0.00	0.00	0.00	0.94
LOI	1.53	1.24	1.11	1.33	1.24	0.65	0.78	0.78	1.71	1.84
Total	100.04	100.00	99.69	99.12	99.86	100.23	100.20	100.06	100.03	100.21
ppm										
Rb	120	154	129	120	124	139	143	130	191	124
Ba	1170	1140	980	1150	1040	1480	1080	1150	800	710
Sr	190	205	200	307	303	319	326	325	132	107
Nb	10	14	35	21	20	18	21	19	9	11
Zr	199	291	515	406	367	371	414	378	207	190
Hf	12	17	27	23	20	21	22	22	12	11
Y	43	41	56	41	37	36	49	40	31	39
Ga	39	41	37	36	35	36	37	42	42	37
Zn	56	104	43	13	14	18	27	43	48	31
Cu	13	18	5	3	0	3	3	4	8	4
Ni	15	35	13	58	10	6	26	18	24	18
Co	10	9	5	3	3	5	4	6	7	8
Cr	18	35	67	37	3	6	8	6	55	15
V	35	58	48	30	31	31	41	43	79	15
Sc	11	14	13	11	9	11	14	12	11	6
La	39	46	94	102	66	29	57	59	23	58
Ce	80	124	209	200	97	54	109	109	42	121
Nd	34	47	74	71	38	25	42	42	22	47
Pb	69	67	56	59	58	57	63	70	70	77
Th	17	21	36	15	15	11	15	14	10	14
U	1	3	6	3	3	4	3	2	0	5

and three-phase aqueous–carbonic fluid inclusions of the LLV-type in amphibolite-facies rocks further south (Bedretto, Cavagnoli and Faido). Consistent phase proportions in all FIA demonstrate that the quartz crystals have trapped a homogeneous fluid, reflected by exceptionally low standard deviations for melting and homogenization temperatures obtained for each fluid inclusion assemblage, and even among all assemblages from a given locality (Table 4, Fig. 7). The two-phase aqueous fluid inclusions showed initial ice melting and final ice melting as well as total homogenization into the liquid phase. The aqueous fluid inclusions from Gauli, Gerstenegg, Tiefengletscher, and Vals never showed any clathrates despite excellent visibility, whereas Miron *et al.* (2013) have observed minor clathrate melting for few large fluid inclusions from Thusis (less than 0.1 vol.% clathrate). The aqueous–carbonic fluid inclusions allowed measurement of final melting of CO_2, final ice melting, final melting of clathrate, partial CO_2 homogenization into the liquid (LLV to LL), and total homogenization into the liquid (LL to L).

The aqueous fluid inclusions have final ice-melting temperatures (Tm_{ice}) of −2.5 to −2.2°C (Thusis), −1.7 to −1.6°C (Vals), −3.0 to −2.6°C (Gauli), −6.7 to −6.5°C (Gerstenegg) and of −6.3 to −5.1°C (Tiefengletscher). They have total homogenization temperatures of 130 ± 2°C (Thusis; Miron *et al.* 2013), 180 ± 10°C (Vals), 151 ± 6°C (Gauli), 185 ± 3°C (Gerstenegg), and 210 ± 7°C (Tiefengletscher). The aqueous–carbonic fluid inclusions have final CO_2 melting temperatures (Tm_{CO_2}) that are only slightly depressed compared to pure CO_2, indicating that the concentrations of additional volatile species such as CH_4 or N_2 are low (Hollister & Burrus 1976; Touret 1982; Thiery *et al.* 1994). The measured

Table 3 Summary of input bulk rock and fluid compositions that were used for fluid–mineral equilibria modeling. For runs with pyrite in excess, 10 g of FeS_2 was added to the bulk composition.

	Gauli	Gerstenegg	Tiefengletscher	Cavagnoli	Faido
Rock part					
SiO_2 (g)	665.35	692.15	692.15	609.77	713.28
Al_2O_3 (g)	182.76	161.16	161.16	213.64	138.00
Fe_2O_3 (g)	9.47	14.77	14.77	27.35	16.39
FeO (g)	4.73	5.78	5.78	2.15	8.07
MgO (g)	4.69	4.82	4.82	6.23	3.85
CaO (g)	26.11	27.92	27.92	3.35	12.19
Na_2O (g)	51.49	48.96	48.96	41.55	43.00
K_2O (g)	43.53	35.95	35.95	78.50	45.87
H_2O (g)	8.86	5.69	5.69	13.90	2.75
CO_2 (g)	0.33	2.60	2.60	0.86	7.11
C (g)	2.68	0.21	0.21	2.69	0.05
S (g)	0	0	0	0	9.45
Au (g)	0.01	0.01	0.01	0.01	0.01
Total	1000	1000	1000	1000	1000
Fluid part					
H_2O (g)	100	100	100	100	100
CO_2 (mol)	0	0	0	1.754364	0.843377
NaCl (mol)	0.084392	0.194386	0.176277	0.006872	0.060228
H_2S (mol)	0.000487	0.002362	0.001821	0.004885	0.007484

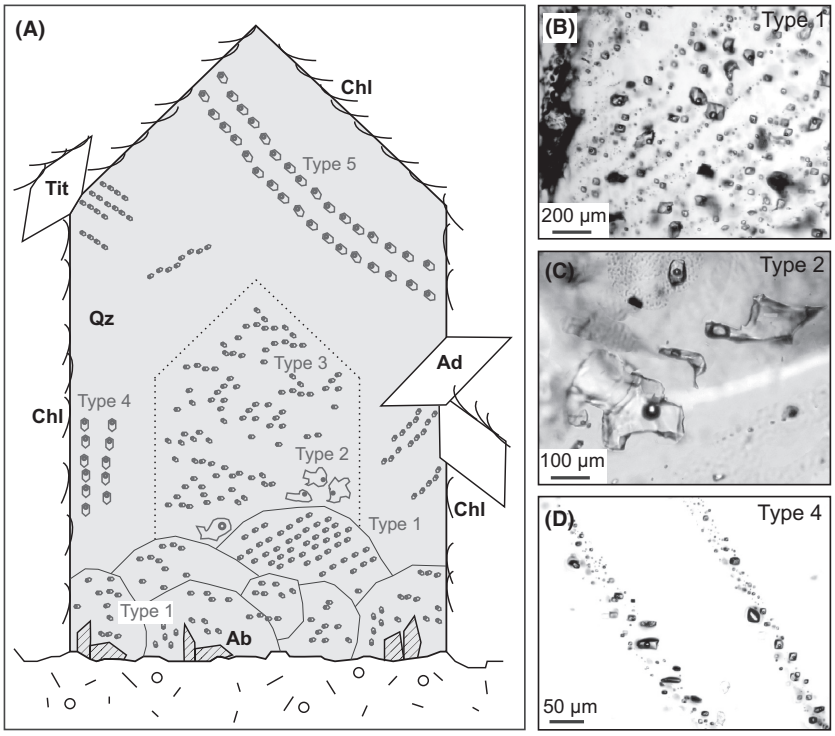

Fig. 4. Typical fluid inclusion assemblages (FIA) from Alpine fissure veins from Gauli and their time relationships. (A) Sketch map showing successive FIA relative to the quartz crystals' growth. The base of the crystal is composed of multiple quartz grains that contain abundant trails of pseudosecondary FIA (Type 1). This zone is followed by growth-zoned quartz hosting numerous pseudosecondary FIA (Type 2 and 3). The outer part of the quartz crystal hosts few pseudosecondary FIA (Type 4) and is crosscut by late trails with secondary FIA (Type 5). (B) Smaller aqueous (LV) fluid inclusions (Type 1) from quartz grains at the base of the crystal, corresponding to FIA A1 to A7 in Table 4. (C) Irregularly shaped aqueous (LV) fluid inclusions (Type 2) located in the central part of the crystal. (D) Trail of pseudosecondary aqueous (LV) fluid inclusions (Type 4) from the outer part of the crystal, corresponding to the FIA A8 to A14 in Table 4, which shows that all inclusion generations have nearly identical properties.

Tm_{CO_2} are in the range of −57.0°C (Bedretto), −57.3 to −57.1°C (Cavagnoli), and −58.2 to −57.9°C (Faido). Final clathrate melting temperatures (Tm_{Cla}) are in the range of 8.9 to 9.8°C (Bedretto), 9.7 to 9.9°C (Cavagnoli), and 9.1 to 9.3°C (Faido). Based on the microthermometric data and estimates of the volume proportions, the X_{CO_2} for the aqueous–carbonic fluid inclusions are calculated as 0.14, 0.13, and 0.13 for Bedretto, Cavagnoli, and Faido, respectively. The average total homogenization temperatures for the aqueous–carbonic fluid inclusions are systematically higher than those of the aqueous fluid inclusions, and are 285 ± 10°C (Bedretto), 295 ± 8°C (Cavagnoli) and 299 ± 12°C (Faido), but they also homogenized into the liquid phase. The aqueous fluid

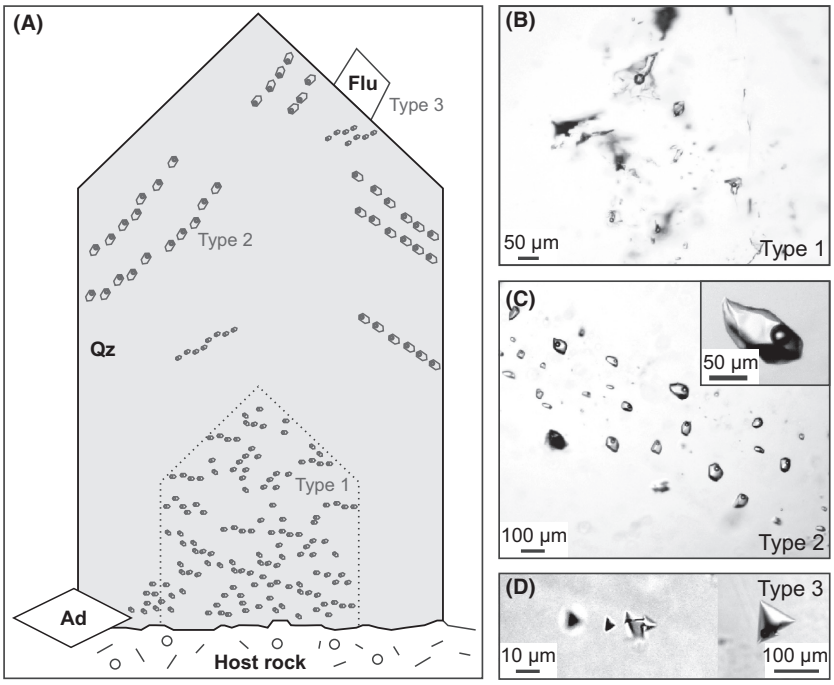

Fig. 5. Fluid inclusion assemblages (FIA) from the Gerstenegg fissure vein and their relative time relationships. (A) Sketch map the time relations of different FIA relative to the quartz crystal growth. The growth-zoned quartz crystals contain pseudosecondary FIA (Type 1) in the central part and mostly secondary FIA (Type 2) in the outer part. The quartz crystals are overgrown by fluorite crystals with very small secondary FIA (Type 3). (B) Irregularly shaped aqueous (LV) fluid inclusions (Type 1) from the central part of the crystal, corresponding to FIA A1 to A3 in Table 4. (C) Trail with secondary aqueous (LV) fluid inclusions (Type 2) from the outer part of the quartz crystals, corresponding to FIA B1 to B3 in Table 4. (D) Small aqueous (LV) fluid inclusions (Type 3) in fluorite.

inclusions show a positive correlation between salinity and temperature of total homogenization (Fig. 7), whereas the aqueous–carbonic fluid inclusions do not show such a relationship.

Elemental composition of fluid inclusions

The elemental composition of 1007 individual fluid inclusions was analyzed by LA-ICPMS (192 from Gauli, 92 from Gerstenegg, 178 from Tiefengletscher, 57 from Vals, 62 from Bedretto, 220 from Cavagnoli, and 206 from Faido). The data were combined with those from Miron *et al.* (2013) and Rauchenstein-Martinek *et al.* (2014). The multi-element fluid inclusion LA-ICPMS data are summarized in Table 4 and illustrated in Figs 8–11 (the full dataset including all microthermometric and LA-ICPMS results for the individual FI grouped by assemblages and fluid inclusion types are listed in the Data S1). The LA-ICPMS fluid inclusion data that were obtained with the short element menu optimized for halogen analysis are listed in Table 5. Figure 8 gives an overview of the elemental concentrations and illustrates that the fluids are compositionally homogeneous at each investigated locality, but that fluid compositions vary considerably between localities.

For all localities, the most abundant cation components are Na, K, and Ca. As expected for low to intermediate salinity fluids, the concentrations of a number of alkaline and alkaline earth elements (Li, K, Rb, Cs, Sr, and Ba) correlate positively with the bulk fluid salinity (Fig. 10) and there are positive correlations among the different alkali metals (Fig. 11). All fluid inclusions contain detectable concentrations of S, As, Sb, and B. The sulfur concentrations increase from north (Thusis: 300 ppm) to south (Faido: 2210 ppm), that is sulfur correlates with the increase in metamorphic grade of the host rocks. Arsenic follows a similar trend, with the highest As contents measured in the low-salinity, high-sulfur inclusions of Cavagnoli (240 ppm). The As concentrations show a good positive correlation with the S concentrations (Fig. 11F) and a fair positive correlation with the Sb concentrations (Fig. 11D). The fluid inclusions from all localities have considerable B concentrations, which are typically on the order of 170 to 960 ppm. The B concentrations do not correlate with fluid salinity or the metamorphic grade and are not systematically different between aqueous and aqueous–carbonic fluid inclusions.

The dataset is more limited for Mg, Fe, and Mn, because in many fluid inclusions, these elements were below their limits of detection. The concentrations of all three elements are typically on the order of few ppm, except in the samples from Tiefengletscher that had an order of magnitude higher concentrations of Fe and Mn. The ore metals Cu, Zn, and Pb were detected in the majority of fluid inclusion assemblages. There are positive correlations between Pb and Zn (Fig. 11E) and between Cu and Zn (Fig. 11G), a feature that has been reported before for Pb and Zn in data compilations for a broad range of crustal fluids (Yardley 2005, 2013).

Table 4 Average elemental composition, melting temperatures (ice, carbon dioxide, and clathrate) and homogenization (carbon dioxide, total) temperatures of all analyzed fluid inclusion assemblages (FIA).

FIA	Type	# FI	Li (ppm)	Na (ppm)	K (ppm)	Rb (ppm)	Cs (ppm)	Mg (ppm)	Ca (ppm)	Sr (ppm)	Ba (ppm)	B (ppm)	Al (ppm)	Fe (ppm)
Gauli														
A1	1	7	180	14400	4340	30	7.7		1560	36	4.0	650	83	
A2	1	3	210	15100	3850	34	7.6	0.20	870	38	4.4	550		
A3	1	7	230	13800	3860	30	7.0	0.27	1660	37	4.2	540	24	
A4	1	4	200	14300	4160	31	7.3		1650	36	4.8	710	44	
A5	1	4	250	13100	3270	24	5.7		4870	42	4.1	420	73	
A6	1	4	150	14800	3310	28	5.9		1360	45	3.4	480		
A7	1	1	130	11900	4510	26	6.9		3270	15	1.8	600	13	
A8	4	18	160	14800	4520	31	7.2		1520	34	5.3	650	62	
A9	4	3	180	14100	2370	23	3.2		5400	68	6.4	460	30	
A10	4	3	160	15200	4530	31	8.9		560	20	3.2	680	49	
A11	2	9	110	14500	3950	29	7.1		1710	41	4.2	680	53	
A12	2	2	140	15000	3220	36	6.8		2440	35	7.0	510		
A13	2	1	140	15800	2160	30	4.4		1090	52	7.2	600	200	
A14	2	10	120	14100	3660	24	6.5		2450	30	3.6	510	54	
B1	3	9	100	14700	4400	12	2.8	11	810	13	10	550	32	
C1	3	5	160	15100	4700	34	7.8	0.51	930	43	4.6	580	43	
C2	3	2	150	14700	2750	27	6.4	0.45	2230	67	6.0	540	46	
C3	3	1	150	15100	4110	33	7.9		1160	39	4.8	600	5.6	
C4	3	3	140	15100	4050	31	6.8		1840	51	4.6	550	5.0	
C5	3	5	120	14600	4250	37	8.7	0.26	1540	45	4.4	640	43	
C6	3	4	150	14800	4950	36	7.7	0.01	1010	25	2.1	610	48	46
C7	3	2	160	15100	4690	34	8.6		890	34	3.8	670	14	
C8	3	3	120	15200	3930	33	7.7		1240	42	4.6	580	52	
Gerstenegg														
A1	1	13	160	26700	9780	140	26	5.0	5750	230	34	380	36	23
A2	1	11	170	27570	7950	130	34	6.6	7560	260	35	350	61	23
A3	1	2	150	29200	5620	87	28	1.8	9700	290	32	310	24	54
B1	2	10	160	28000	9450	130	24	10	5520	200	25	310	20	94
B2	2	6	150	24000	8100	91	33	8.1	8700	210	37	260		
B3	2	6	220	27300	8410	130	25	6.1	6400	250	33	300	90	14
C1	2	7	200	34000	8790	35	6.4	6.7	1770	110	110	200		
C2	2	4	130	27400	5820	90	21	6.3	8480	290	31	290	43	
C3	2	2	160	33500	8990	35	6.7		3080	180	170	270		
Tiefengletscher														
A1	1	7	220	28600	11000	81	13	3.8	1740	55	21	250	81	99
A2	1	3	250	28000	11100	84	9.2		2620	33	23	250	57	150
A3	1	7	230	28500	9870	95	13	4.0	1810	98	19	210	10	52
A4		8	260	27300	12000	88	15	1.5	1800	30	22	280	68	140
B1	2	8	240	26700	13600	76	12	4.6	1800	34	22	230	32	51
B2	2	4	230	26500	13000	74	11	5.1	1580	32	20	220	130	80
B3	2	9	260	27600	12200	100	16	4.6	1980	91	16	250	34	100
B4	2	3	230	27100	12400	85	12	3.6	2030	81	20	260	130	70
B5	2	3	230	27800	11500	88	17	2.5	1930	88	10	250	3.6	67
B6	2	1	260	22400	19300	59	12	1.4	2630	22	21	170		180
C1	3	3	260	28600	12700	75	14	2.0	910	39	22	290	38	140
C2	3	4	260	27200	8790	54	10	6.9	3290	95	76	200	110	130
C3	3	4	240	28400	10700	62	10	1.6	1600	45	25	230	64	84
C4	3	3	250	28400	12200	76	13	3.0	1550	36	23	260	50	94
C5	3	6	260	25800	11700	100	14	1.5	1900	66	25	260	46	160
C6	3	2	290	27300	12500	88	13		1880	37	28	340	41	100
C7	3	1	230	23100	10900	60	8.7	12	6350	29	15	250	110	180
C8	3	1	220	27800	12300	89	15	1.6	1510	38	22	250	36	57
Cavagnoli														
A1	1	7	7	680	22	0.32	0.15	4.1	730	0.05	0.2	200	23	3
A2	1	4	7	760		0.3	0.17	4.4	610	0.05		240	16	
A3	1	2	9	1010	67	0.8	0.18		430	0.20	0.4	300	82	
A4	1	2	4	1260		0.7	0.80			0.18		410	6.0	
A5	1	1	3	500	93	0.5	0.11		660	3.1		180		
A6	1	7	4	1080		0.7	0.29		580	0.27		330	27	
B1	1	4	12	630	39	0.4	0.23		980	0.02	0.5	140	48	
B2	1	9	49	1020	76	0.6	0.19			0.27		260	71	
B3	1	4	4	1020	63	0.5	0.52	2.2		0.02	0.9	370	75	8
B4	1	3	9	1100	70	0.7	0.31			0.27	1.4	350	160	
B5	1	1		1250	94	0.8	0.20	1.1			0.5	320	71	

Mn (ppm)	Cu (ppm)	Zn (ppm)	Pb (ppm)	Ag (ppm)	As (ppm)	Sb (ppm)	Ti (ppm)	S (ppm)	Cl (ppm)	Br (ppm)	Tm_{CO_2} (°C)	Tm_{Ice} (°C)	Tm_{Cla} (°C)	Th_{CO_2} (°C)	Th_{tot} (°C)
13	2.5	11	0.43	0.07	3.8	7.1		420	35000	290		−2.9			150
3.0		2.0	0.14		1.1	3.5		280	29200	180		−2.9			149
	2.2	6.8	0.49		1.5	7.3		160	28900	160		−2.9			153
11					1.0	7.0		230	27200	130		−2.8			
					3.4	10		410	32900	100		−2.8			
2.4				0.28	0.93	4.3		220	25400	150		−2.8			
					3.0				20500	98		−2.8			
		13	0.47		5.3	7.0	15	360	31400	220		−2.8			146
			0.59						27400	140		−2.8			
		6.0	0.39		2.7	7.1		390	32600	77		−2.8			
		16	0.77	0.38	7.3	8.7		400	30200			−2.7			143
					5.0			890	25300	280		−2.8			
		21							44200			−2.8			
	5.5	20		0.57	9.8		20	610	29400	200		−2.8			153
6.0						7.8		340	27900	190		−2.6			145
						3.3	1.5	140	24200	81		−2.7			144
0.6						1.2		71	24600	40		−2.8			146
						3.0		140	27600	46		−2.7			146
						2.3	1.4	340	29100	120		−2.7			144
0.4						2.4	0.58	160	31400	110		−2.8			148
						3.5		180	28200	73		−2.7			163
						3.2	0.82	170	26700	45		−2.8			
0.3						2.9	1.3	160	26900	52		−2.8			
23		6.0	6.0	1.0	40	1.0	3	150	52500	210		−6.6			185
15		200	2.1	1.4	17	0.85	6.2	270	61500	350		−6.9			185
2.2			0.44	0.19	2.5	0.54		320	57300	180		−6.6			185
19	8.6	41	4.6	1.0	35	3.8	24	190	52900	680		−6.5			187
11	10	21	3.1		15		36	570	42900	750		−6.5			186
19	47	61	11	1.7	29	2.6	24	1440	41700	1100		−6.5			
42	53	36	28		34	6.1	61	930	52300	630		−6.6			186
12			7.5		15	3.3			43900	420		−6.7			
			58		38				53300	240		−6.5			
49	160	14	38	1.0	49	4.5	3.1	390	50700	220		−6.0			208
64	200	45	64	0.71	56	5.9		640	52500	230		−6.2			
46	93	13	26	0.70	42	5.6	2.1	320	48600	130		−6.2			208
82	270	36	52	1.8	58	10	1.6	550	45700	240		−6.1			
54	190	17	39	1.0	43	2.8	4.4	670	50700	210		−6.1			216
62	180	14	38	0.63	44	2.4	3.0	620	43100	130		−6.2			
55	150	14	41	0.86	63	3.1	3.0	430	50700	130		−6.1			215
57	130	16	33	0.40	47	2.7	5.9	250	44600	200		−5.9			
56	92	20	50	0.64	57	4.6	2.0	290	52300	110		−6.2			
190	230	17	63	0.76	92	4.3		170	51700	820		−6.2			
78	220	10	42	1.0	56	3.1	2.0	660	52300	180		−6.2			211
82	56	23	38	0.24	44	4.1	8.4	180	46300	220		−6.2			
59	130	20	38	1.1	42	3.3	13	550	49600	280		−6.2			212
71	220	13	39	1.0	60	3.0		700	45500	220		−6.3			202
90	300	28	51	1.7	80	3.6	17	910	43600	300		−6.1			
76	190	25	63	1.6	85	7.2	1.2	660		200		−6.1			
82	150	27	34	0.78	48				34400	270		−6.1			
56	190	14	39	0.83	44	3.4		510		76		−6.1			
	1.5	5.6	0.08	0.24	82	1.4	18	510			−57.0		9.9	27.4	
			0.08	0.03	170	4.1		630	290		−57.0		9.9	26.8	
					250	6.3	25	870			−57.0		9.8		
			0.04		150	4.3		910	270		−57.1		9.9		
18	12	27	2.9	0.64	130	5.1		820					9.9		
				0.24	200	4.7		450	340		−57.0		9.9	28.1	295
		0.5	0.10		110	2.9		500			−57.1		9.9	27.5	
		2.9	0.55	0.35	190	5.5		870	3740	170	−57.0		9.9		
	0.6	0.5	0.17	0.09	280	6.0		1120			−57.1		9.9	26.9	
		2.5	0.36	0.12	270	4.3		900			−57.1		9.9		
					240	7.0		930			−57.0		9.8		

Table 4 Continued.

FIA	Type	# FI	Li (ppm)	Na (ppm)	K (ppm)	Rb (ppm)	Cs (ppm)	Mg (ppm)	Ca (ppm)	Sr (ppm)	Ba (ppm)	B (ppm)	Al (ppm)	Fe (ppm)
B6	1	1		1270	61	0.7	0.24			0.08		380	27	
B7	1	7	9	1020	63	0.9	0.43	4.8		0.09	2.0	330		
C1	2	10	14	910	72	0.7	0.64	0.7		0.28	1.4	320	31	10
C2	2	7	15	860	94	1.2	0.46	0.7	260		2.4	430	17	58
C3	2	2	11	1030	78	0.7	0.17					470	49	
D1	3	4	21	1060	25	0.6	0.33	11.7				340	57	
D2	3	3	5	1060	44	0.6	0.30	1.8		0.45		430		
D3	3	8	7	730	57	0.7	0.22	0.7				270	10	
D4	3	6	9	1000	74	0.6	0.68				1.3	380	30	
D5	3	1	5	1070		0.5	0.41					320	33	
D6	3	1	2	1060	46	0.6	0.36					470	18	
Faido														
A1	1	4	50	5730	1930	38	12	4.1		7.0	2.3	450	84	37
A2	1	9	28	10100	2750	18	5	1.9	280	3.8	3.4	860	54	110
A3	1	2	30	11200	1650	15	30	2.6	55	17	6.1	410	17	63
A4	1	3	23	9550	2330	27	14	14	41	7.3	1.7	650		23
B1	2	9	33	9140	2920	24	17	3.5	1500	5.1	2.4	560	150	63
B2	2	6	25	10600	2490	22	20	0.6	430	7.1	1.2	700	110	59
B3	2	2	26	10500	2940	21	4			1.7	0.3	970	25	82
B4	2	4	26	9940	2300	16	19	1.1	1580	8.4	1.2	670	41	86
B5	2	6	54	10600	2420	19	10	6.7	540	9.7	4.0	720	100	77
B6	2	4	36	10500	2850	26	20	1.9		7.1	1.9	830	98	160
B7	3	5	28	10100	3050	18	4	0.9	390	1.3		930	120	61
B8	3	3	18	10800	2240	26	29	3.6	96	9.5	1.0	410	140	
B9	3	3	23	9340	2360	24	13	43	1270	5.7	1.9	550	34	
B10	3	3	25	9950	2710	26	12	69	1700	5.7		540	140	
B11	3	5	25	10200	2680	21	21	1.0	840	9.3	1.7	550	110	190

The complete dataset is provided in the Data S1.

Concentrations of Al and Ti are in the range of 45–89 ppm and 5–26 ppm, respectively, in all investigated FIA's. Both elements do not show any clear correlation with salinity and the lithology of the host rock. Titanium is also present as trace element (1–5 ppm) in the quartz hosting the fluid inclusions, and it was therefore only possible to quantify Ti concentrations in some fluid inclusions where we observed a well-defined Ti peak that closely followed the shape of the large Na peak. The Ti and Al in the host quartz were monitored immediately before breaching the fluid inclusions and after the inclusion was opened, and we can subtract the host background and reliably quantify concentrations in inclusions where clear peaks significantly above the host background were detected.

The concentrations of Cl and Br were analyzed as part of the multi-element menu, but we also performed additional measurements on fluid inclusions from selected assemblages with an element menu that was optimized for higher precision analysis of the Cl/Br ratio (Seo *et al.* 2011). The plot of the molar Cl/Br ratios (Fig. 9) shows that the measurements with the shorter optimized element menu have smaller analytical errors, but that the average Cl/Br ratio of the fluid from each fissure vein is essentially the same for both sets of analyses (Fig. 9). Measured Cl and Br concentrations in each inclusion were first converted into molar values. The molar Cl/Br ratios were then averaged for each fluid inclusion assemblage and also for all assemblages from each fissure vein. Average molar Cl/Br values are 350 ± 160 for Gauli, 440 ± 200 for Gerstenegg, and 510 ± 30 for Tiefengletscher, whereas average values are 100 ± 55 for Cavagnoli, 20 ± 30 for Bedretto, and 140 ± 50 for Faido.

FLUID–ROCK EQUILIBRIA MODELING AND PRESSURE–TEMPERATURE EVOLUTION

We have combined chemical solute thermometry, fluid inclusion isochores, and constraints from fluid–mineral equilibria modeling to estimate the pressure–temperature conditions of the Alpine fissure veins and to compare these with published data for the metamorphic P-T path of their host rocks. The peak metamorphic conditions of the host rocks were adopted from Todd & Engi (1997). They are 430–470°C and 4–6 kbar for Gauli, 420–460°C and 3–5 kbar for Gerstenegg, 420–480°C and 3–5 kbar for Tiefengletscher, 460–530°C and 5–7 kbar for Cavagnoli, and 530–600°C and 5–7 kbar for Faido (Fig. 14).

As fluid inclusion microthermometry provides only minimum temperatures and P-T slopes (obtained from

Mn (ppm)	Cu (ppm)	Zn (ppm)	Pb (ppm)	Ag (ppm)	As (ppm)	Sb (ppm)	Ti (ppm)	S (ppm)	Cl (ppm)	Br (ppm)	Tm_{CO_2} (°C)	Tm_{ice} (°C)	Tm_{Cla} (°C)	Th_{CO_2} (°C)	Th_{tot} (°C)
		1.8	1.0		290	9.5		1260		82	−57.0		9.9		
		1.5	1.5	0.13	300	6.0		1170		110	−57.0		9.9	27.4	299
	1.5		0.78	0.36	230	5.0	4.8	1030	1480	19	−57.0		9.9	26.0	
	3.4	1.7	0.59		420	10	3.8	2950	600		−57.1		9.8	27.4	303
	0.9		0.77	0.10	350	11	2.0	1880	520		−57.2				
	2.1		1.5		410	6.5		1920			−57.0		9.9		
			0.27		340	8.9		1420			−57.1				
	2.9	1.6	0.33		200	5.2		770			−57.0		9.9	25.9	
	2.4				350	14		2940			−57.0		9.9		
					200	3.3		800			−57.1		9.8	25.9	
			0.85		370	9.0		1590			−57.0		9.9		
16	35	16	20	0.74	88	2.6	19	1180	11200	210	−58.2		9.3	26.2	300
34	100	30	40	1.5	140	1.8	8.1	2740	11600	260	−58.2		9.2	28.0	299
	84	7.0	24		1.0	0.5	1.9	190	13900	150	−57.9		9.3	28.3	
2.1	4	4.5	33	0.09	91	3.0	33	1570	11300	350	−58.0		9.3	28.4	
16	66	20	22	1.1	120	3.1	7.3	1660	10300	290	−58.2		9.2	29.2	294
14	130	46	31	2.1	110	1.9	20	2050	12800	240	−58.1		9.2	26.5	
3.2	210	49	43	2.7	160	1.5	6.0	4100	11300	120	−58.2		9.3		
61	150	43	67	2.7	200	3.3		2930	13600	400	−58.2		9.3	26.2	302
60	100	36	42	1.7	140	3.5	10	3380	8340	380	−57.9		9.2	28.7	307
39	65	49	33	1.2	150	1.2		2720	14100	250	−58.2		9.2	26.9	
66	150	52	49	2.3	160	3.4		3290	9710	260	−58.0		9.3	26.8	313
	1.6	5.8	7.0		43	1.0	15	630	13400	290	−58.1		9.2		
23	7.0	5.8	5.0	1.1	130	3.0	3.4	1620	9790	400	−58.2		9.2		
21	14	14	9.0		150	2.3	28	2080	13500	270	−58.2		9.3		
20	26	13	11		98	1.8		1300	13200	270	−58.1		9.2	29.1	

isochores calculated from the fluid densities), additional independent temperature or pressure information is required for evaluating the conditions of fluid inclusion entrapment and vein formation. Commonly, geothermometry of vein and host-rock minerals is used to provide this temperature information, which is then combined with isochores calculated from fluid inclusion data (Goldstein & Reynolds 1994; Bakker 2003). This approach relies on the presence of appropriate mineral assemblage that are suitable as geothermometers and requires that the relative timing of vein minerals can be unequivocally linked to that of fluid inclusion assemblages.

Alternatively, chemical solute thermometers that are routinely used for geothermometry of active thermal springs and geothermal systems (Arnorsson 2000) can be applied to fluid inclusion compositions (Mullis *et al.* 1994; Marsala *et al.* 2013; Miron *et al.* 2013). We have used the Na-K (Giggenbach 1988), Na-Li (Kharaka *et al.* 1982), Li-Mg (Kharaka & Mariner 1989), K-Mg (Giggenbach 1988), Na-Mg (Giggenbach 1988), Na-K-Ca (Fournier & Truesdell 1973), and Na-K-Mg (Nieva & Nieva 1987) geothermometers. For most vein locations, the Na-K and Na-Li thermometers gave consistent results and a comparatively narrow range in temperatures (Table 6). The geothermometers relying on Mg and Ca concentrations yielded reasonable temperatures for some locations, but for other locations (Cavagnoli and Faido) gave results that were inconsistent with fluid inclusion homogenization and other temperature estimates. This is due to the high analytical uncertainties associated with the LA-ICPMS measurements of Mg and Ca. Solute geothermometry was not successful for the Cavagnoli data, because all geothermometers gave temperatures that were below the fluid inclusion homogenization temperatures or just overlapped with them. This reflects the low total elemental concentrations and related large analytical uncertainties for these very low salinity (0.4 wt.% eqv. NaCl) aqueous–carbonic fluid inclusions.

The estimates of Alpine fissure vein formation temperatures were therefore based on the Na-K and Na-Li solute thermometers (Table 6). For the Gauli, Gerstenegg, and Tiefengletscher veins, we accepted the total range in temperature obtained from both the Na-K and Na-Li thermometers. For the Cavagnoli and Faido veins, we discarded temperatures that were below the average value of the fluid inclusion homogenization temperatures (295 and 299°C for Cavagnoli and Faido) and accepted the range in temperature above 300°C from the Na-K and Na-Li thermometers. This resulted in estimates for the vein formation temperatures of 280–380°C for Gauli, 250–350°C for Gerstenegg, 350–440°C for

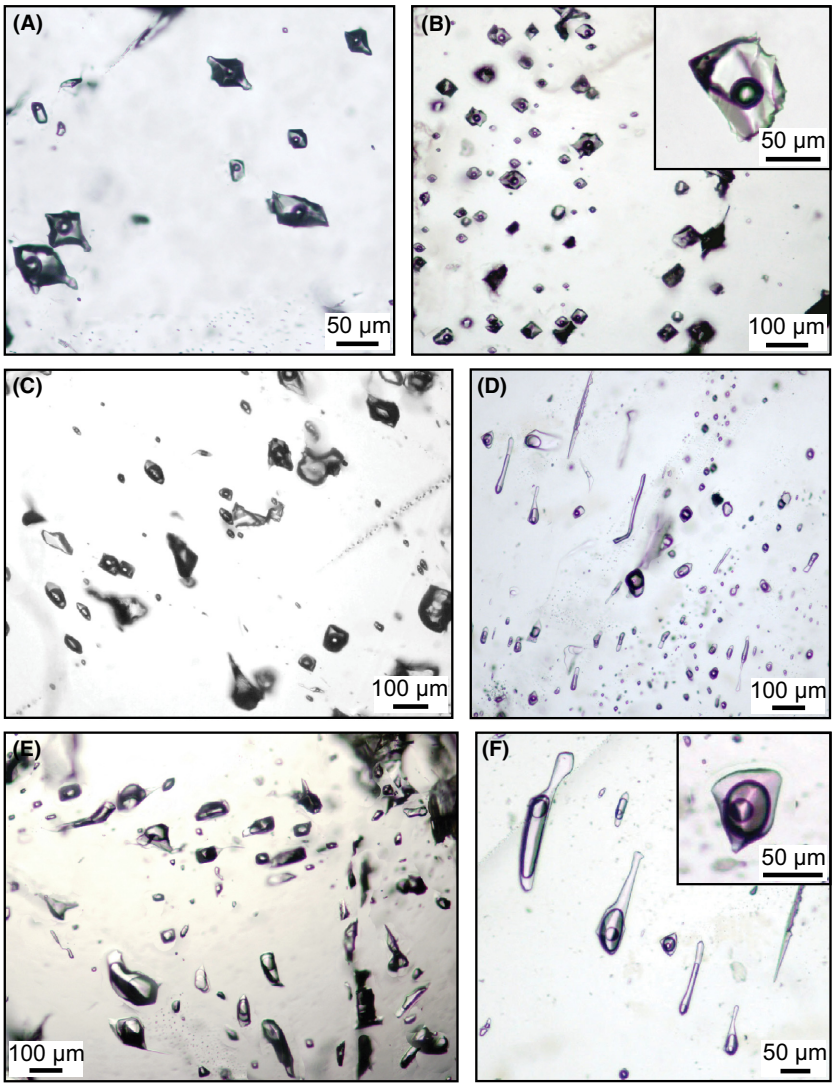

Fig. 6. Photographs of typical fluid inclusion assemblages (FIA). (A) Characteristic regularly shaped aqueous (LV) fluid inclusions from Vals (FIA A2). (B) Characteristic regularly shaped aqueous (LV) fluid inclusions from Tiefengletscher (FIA A4). (C) Trail of aqueous–carbonic (LLV) fluid inclusions from Faido (FIA B1). (D) Several subparallel trails of aqueous–carbonic (LLV) fluid inclusions from Cavagnoli. (E) Irregularly shaped aqueous–carbonic (LLV) fluid inclusions from Bedretto (FIA A2). (F) Trail of elongate aqueous–carbonic (LLV) fluid inclusions from Cavagnoli (FIA B3).

Tiefengletscher, 300–360°C for Cavagnoli, and 300–360°C for Faido. Pressure estimates for each fissure vein were then obtained by combining the temperature ranges calculated by solute geothermometry with fluid inclusion isochores for the same FIA. This results in estimates for the vein formation pressures of 2.2–4.7 kbar for Gauli, 1.0–3.2 kbar for Gerstenegg, 2.1–4.1 kbar for Tiefengletscher, 1.4–3.0 kbar for Cavagnoli, and 1.5–3.1 kbar for Faido (Fig. 14).

Additional and potentially better P-T constraints can be obtained from the results of multicomponent fluid–mineral equilibria modeling (e.g., Spycher *et al.* 2014). We have modeled the fluid equilibrium speciation and rock composition (mineralogy and mineral abundance) over the temperature range 200–600°C and at the pressure that represents the average value of the range obtained from the fluid inclusion geothermobarometry (solute thermometers and isochores). Because exploratory fluid–mineral equilibria calculations have shown that the relevant mineral stability boundaries are not very sensitive to pressure, we performed calculations for fixed pressures (3.0 kbar for Gauli, 2.5 kbar for Gerstenegg, 3.0 kbar for Tiefengletscher, 1.8 kbar for Cavagnoli, and 2.0 kbar for Faido). The modeled wall-rock mineralogy and mineral abundance were compared to the minerals identified by petrography.

The complete mineral abundance and fluid composition results are plotted for two examples in Fig. 12 (Tiefengletscher and Faido), and Fig. 13 shows the predicted mineralogy as function of temperature for all five localities. The modeled element ratios in the fluid such as K/Na, Ca/Na, Mg/Na, and Mg/K were compared to those determined by LA-ICPMS analysis of fluid inclusions (Fig. 12). The temperature range of overlap is used for estimating vein formation temperature (Fig. 14). We then combined these temperature

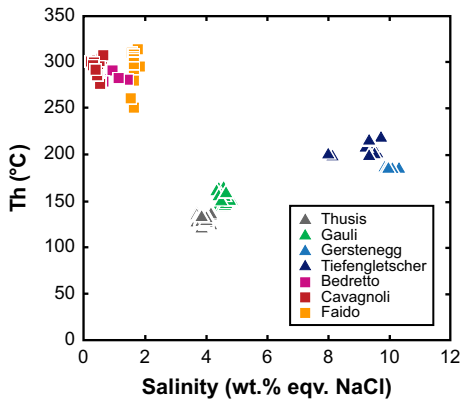

Fig. 7. Plot of salinity (wt.% equivalent NaCl) vs. total homogenization temperature (Th_{tot}) for all locations. Each data point represents the average value for one fluid inclusion assemblage (FIA). Data for Thusis are from Miron *et al.* (2013). Standard deviations within one FI are slightly larger than the symbol size, showing that fluid properties at each location are constant across several stages of entrapment according to petrographic relations. The aqueous fluid inclusions show a broadly positive correlation between salinity and homogenization temperatures, whereas the aqueous–carbonic fluid inclusions do not show such a correlation.

ranges with the isochores for fluid inclusions from each Alpine fissure vein, to obtain our best estimates for the pressure–temperature conditions for fluid inclusion entrapment and Alpine vein formation, that is, 320–380°C and 2.8–4.6 kbar for Gauli, 330–350°C and 2.2–3.2 kbar for Gerstenegg, 350–430°C and 2.1–3.9 kbar for Tiefengletscher, 300–350°C and 1.4–2.9 kbar for Cavagnoli, and 300–340°C and 1.5–2.8 kbar for Faido.

DISCUSSION AND CONCLUSIONS

Fluid sources

The regional correlation of metamorphic grade with the major-component composition of fissure vein fluids indicates a fluid source related to prograde Alpine metamorphism (Mullis *et al.* 1994; Mullis 1996). On the other hand, the occurrence of the largest fissure veins in previously metamorphosed granites subject to retrograde greenschist-facies metamorphism during the Alpine orogeny (Gerstenegg and Tiefengletscher in the Aar massif) requires a fluid source outside of the local host rock. The detailed microthermometric and LA-ICPMS data from eight fissure veins reported here demonstrate that the fluid inclusions in Alpine fissure veins were trapped from compositionally variable, but locally exceptionally homogeneous fluids. Throughout the entire sequence of quartz crystal growth and fluid inclusion entrapment at each location, encompassing several generations of texturally pseudosecondary FI in different growth zones and later secondary FI on crosscutting healed fractures, essentially the same fluid has been present. The chemical geothermometry and the results of fluid–mineral equilibria modeling support the conclusion that wall-rock leaching, mineral precipitation in the fissure veins, and fluid inclusion entrapment proceeded under rock-buffered conditions that closely approached fluid–rock equilibrium at the scale of the local host rock unit. Therefore, the concentrations of most chemical components in the fluid (notably the major and minor cations that are dictated by fluid–mineral equilibria with rock-forming minerals such as feldspars, micas, and ferromagnesian minerals) cannot inform us about the ultimate source of the fluids. The same evidence applies to oxygen isotope compositions of quartz crystals, which were previously shown to be completely buffered by quartz in the local host rock (Sharp *et al.* 2005). Chemical components that preferentially partition into the fluid phase, such as halogens, carbon, hydrogen, and possibly arsenic and boron have a better chance of preserving information about the ultimate fluid source (Ridley & Diamond 2000).

The halogen elements, chlorine, bromine, and iodine, are among the most popular tracers for distal fluid sources, because their concentrations are several orders of magnitude higher in saline fluids (2.03 wt.% Cl and 69.7 ppm Br in seawater) than in crustal rocks (244 ppm Cl and 0.88 ppm Br for the average continental crust; Rudnick & Gao 2004), and they are not easily incorporated into rock-forming minerals during fluid–rock interaction and hydrothermal alteration (Banks *et al.* 1991; Heinrich *et al.* 1993; Yardley *et al.* 1993; Meere & Banks 1997; McCaig *et al.* 2000). The Cl/Br ratios of fluid inclusions have been used to discriminate between several principal fluid sources such as seawater (molar Cl/Br ratio: 640; McCaffrey *et al.* 1987), evaporated seawater (Cl/Br ratio: lower than seawater), and fluids that have dissolved halite (Cl/Br ratio: higher than seawater) from evaporite sediments (Chi & Savard 1997; Stober & Bucher 1999; Yardley 2013).

Considering only our higher quality data obtained with the optimized element menu, the average molar Cl/Br values of all analyzed Alpine fissure fluids are consistently below the seawater value of 640. The fluids trapped in fissure veins of the Aar massif have moderately depleted Cl/Br between 300 and 600, whereas values in the amphibolite-facies Penninic nappes are even lower between 50 and 200 (Fig. 9). Such data would be conventionally interpreted by involvement of evaporated seawater (residual bittterns), which may appear possible considering that evaporites form part of the upper crustal Alpine nappe stack (Berger *et al.* 2005; Wiederkehr *et al.* 2009, 2011). However, the lowest Cl/Br ratios would require extreme evaporation of seawater, by removal of

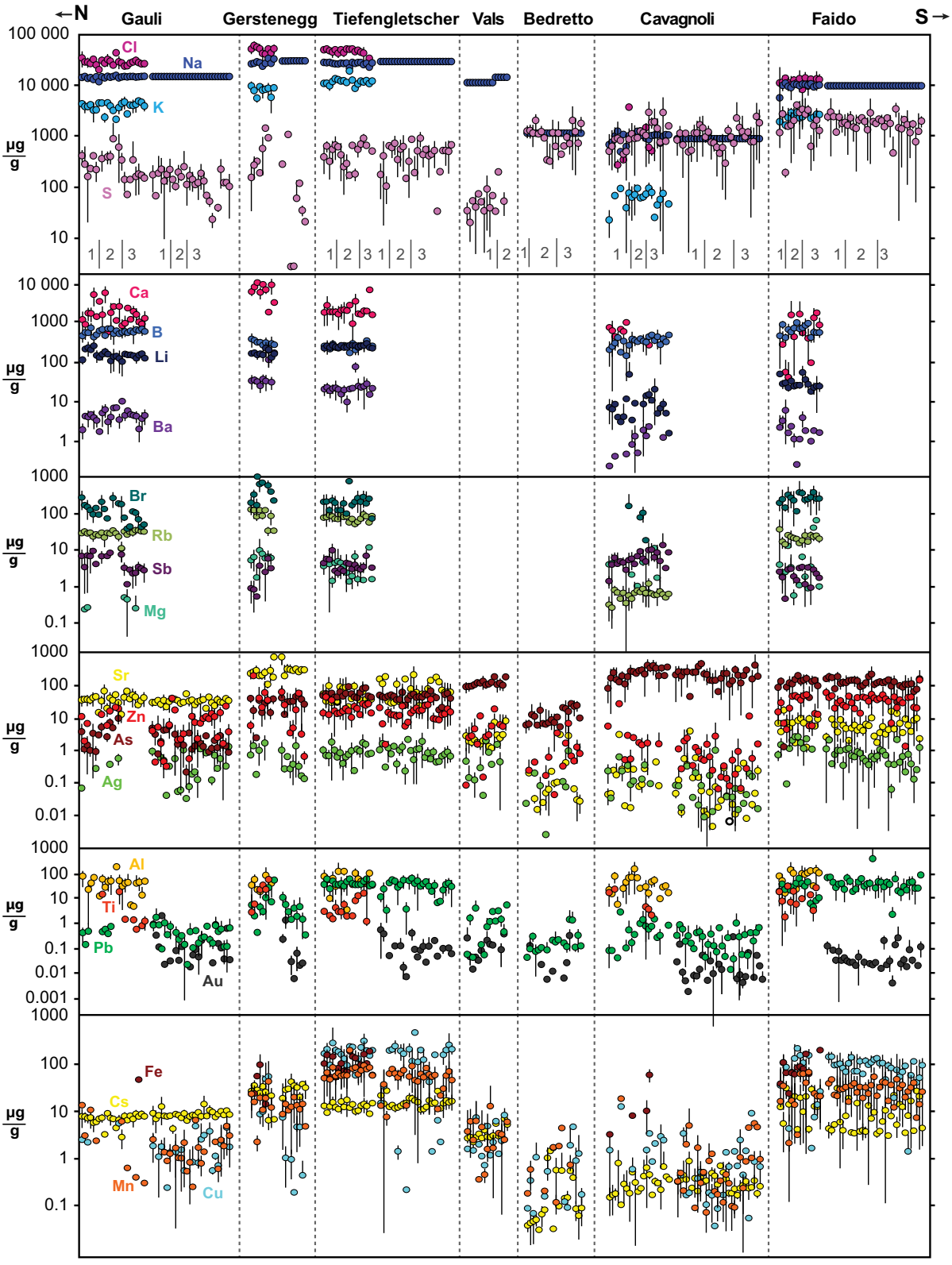

Fig. 8. Summary plot of the average composition of fluid inclusion assemblages analyzed by LA-ICPMS from all investigated Alpine fissure veins (error bars are ± 1σ standard deviation within each FIA). Data for each locality are sorted according to relative age of fluid inclusion assemblages (1: earliest pseudosecondary FIA in the core of the quartz crystals; 2: younger FIA, either pseudosecondary FIA in late growth zones of quartz crystals or secondary FIA that cross-cut through all growth zones; 3: texturally pseudosecondary or secondary FIA with ambiguous time relationships).

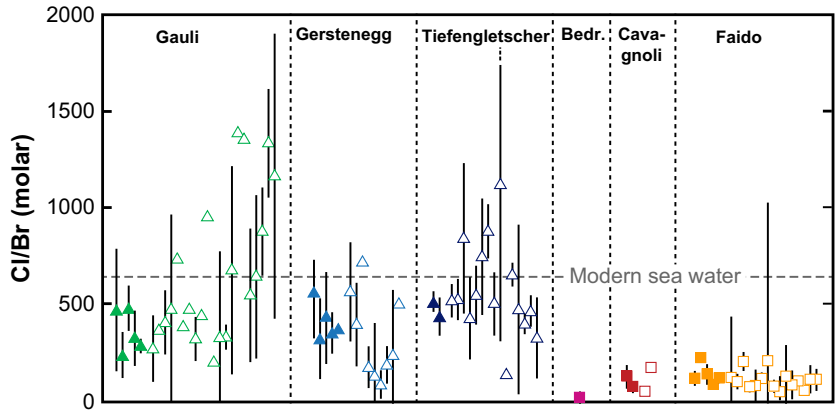

Fig. 9. Summary diagram of the molar Cl/Br ratios obtained from FIA from Gauli, Gerstenegg, Tiefengletscher, Bedretto, Cavagnoli, and Faido. All data points are assemblage averages with error bars of ± 1σ standard deviation, no error bars indicate that only one inclusion was measured above the limits of detection for both Br and Cl. Open symbols are data obtained with the multi-element menu, while full symbols are data obtained with the shorter element menu optimized for halogen analysis (see Seo *et al.* 2011). The seawater value (640) is given for reference.

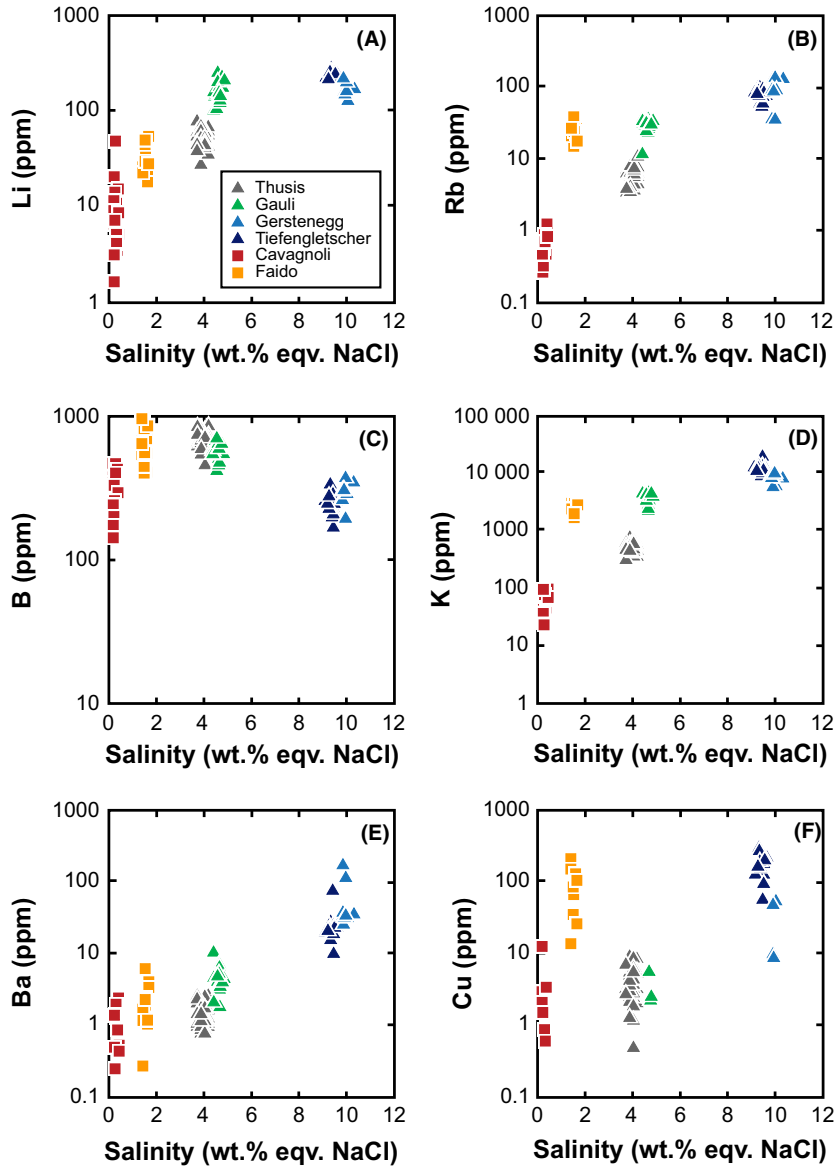

Fig. 10. Variation of (A) lithium, (B) rubidium, (C) boron, (D) potassium, (E) barium, and (F) copper concentrations as function of bulk fluid salinity (expressed as wt.% equivalent NaCl). The three alkali metals (Li, Rb, and K) and Ba show a positive correlation with salinity, whereas B concentrations are broadly negatively correlated with salinity.

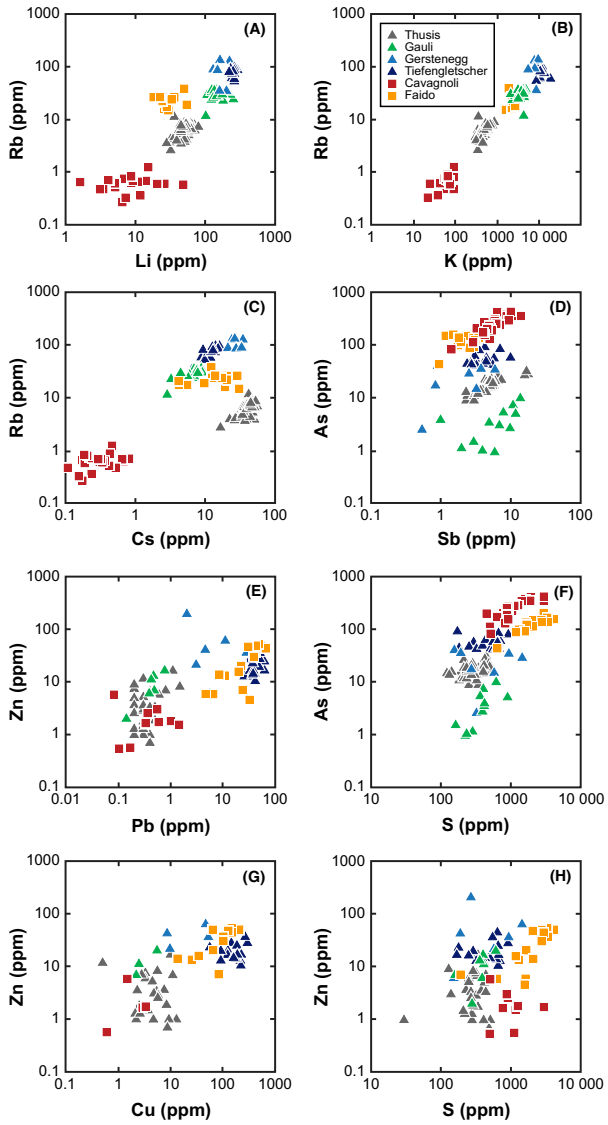

Fig. 11. Variation diagrams for fluid inclusion compositions, with each data point representing the average of one FIA. (A) Rb as function of Li; (B) Rb as function of K; (C) Rb as function of Cs; (D) As as function of Sb; (E) Zn as function of Pb; (F) As as function of S; (G) Zn as function of Cu; (H) Zn as function of S. Squares are aqueous–carbonic and triangles are aqueous inclusions differentiated by colors according to localities.

Table 5 Average elemental composition for the short element menu and the calculated Cl/Br molar ratios for the measured fluid inclusion assemblages (FIAs).

FIA	# FI	Na (ppm)	Rb (ppm)	Cl (ppm)	Br (ppm)	Cl/Br (by wt)
Gauli						
C1	2	14570	13	16910	90	470
C2	3	14570	10	17460	210	240
C3	3	14570	25	21860	110	480
C4	4	14570	31	21550	190	330
C5	3	14570	29	23650	190	290
Gerstenegg						
C1	2	28630	150	55130	230	580
C2	2	28630	150	53380	470	260
C3	4	28630	150	69190	460	460
C4	3	28630	130	52760	300	450
C5	2	28630	150	72110	430	380
Tiefengletscher						
A1	3	27060	160	54100	230	540
B1	3	27060	150	45630	220	480
Cavagnoli						
A1	10	890	1.4	290	17	130
A2	5	890	0.8	220	12	67
Faido						
B1	2	9840	18	16020	330	120
B2	2	9840	38	15950	160	230
B3	4	9840	40	15080	270	140
B4	2	9840	49	15560	400	85
B5	3	9840	35	13240	260	120
Bedretto						
A2	1	1150		470	60	18

The complete dataset is provided in the Data S1.

>90% of initial marine salts as halite, prior to renewed dilution with salt-free metamorphic water. Such mass balance considerations do not make this interpretation very plausible.

An alternative to explain low Cl/Br ratios in low-salinity fluids is the interaction between metamorphic fluids and Br-enriched organic matter or graphite, which may contain high concentrations of Br (Kendrick *et al.* 2011). Reaction between salty fluids and organic matter can liberate Br and result in a progressive decrease in the Cl/Br along the fluid flow path, leading to pore fluids with Cl/Br ratios resembling those of residual evaporite brines (Kendrick *et al.* 2011). The Cl/Br ratios of fluid inclusions from quartz veins in very-low-grade metasediments of the Rhenish massif (Variscan fold-and-thrust belt) are similarly below seawater ratio and were interpreted by interaction with abundant organic matter, in the absence of any evaporites in the shallow marine sequence of the Rhenish massif (Marsala *et al.* 2013). Given that some of our locations are hosted in organic-bearing calc–mica schists (Thusis, Bedretto), the Cl/Br ratios of the fluid inclusions trapped in the Alpine fissure veins may be interpreted in the same way. The fluids in the Aar Massiv could have been initially produced by metamorphic devolatilization of an underlying wedge of Mesozoic to Oligocene sedimentary rocks, which are locally rich in organic matter and were partly overthrusted during the last phases of Alpine subduction and incipient topographic uplift of the Aar massif (Schmid *et al.* 2004). Preferential retention of Br relative to Cl in organic-rich metasediments could also explain the observation that fluids with the lowest salinity but greatest relative enrichment in Br occur in fissure veins hosted by rocks of the highest metamorphic grade, in fluids where also the more refractory volatile components, CO_2 and H_2S, are enriched.

The measured sulfur concentrations vary over a large range from 10–20 ppm up to 2000 ppm. Sulfur is

Table 6 Summary of the results of solute geothermometry of fluid inclusions, based on LA-ICPMS data. Listed are average values and standard deviations for each solute geothermometer.

Locality	Na-K (°C)*	Na-Li (°C)†	Li-Mg (°C)‡	K-Mg (°C)*	Na-Mg (°C)*	Na-K-Ca (°C)§	Na-K-Mg (°C)¶
Gauli	312 (23)	319 (57)	446 (126)	446 (129)	573 (250)	300 (21)	329 (39)
Gerstenegg	321 (30)	254 (13)	333 (21)	359 (15)	421 (87)	305 (21)	307 (13)
Tiefengletscher	390 (37)	431 (11)	390 (34)	423 (40)	497 (97)	364 (23)	354 (25)
Cavagnoli	178 (33)	300 (65)	196 (33)	133 (30)	58 (29)	108 (34)	157 (28)
Faido	307 (25)	329 (33)	242 (38)	297 (46)	275 (108)	301 (16)	279 (21)

*Giggenbach (1988).†Kharaka *et al.* (1982).‡Kharaka & Mariner (1989).§Fournier & Truesdell (1973).¶Nieva & Nieva (1987).

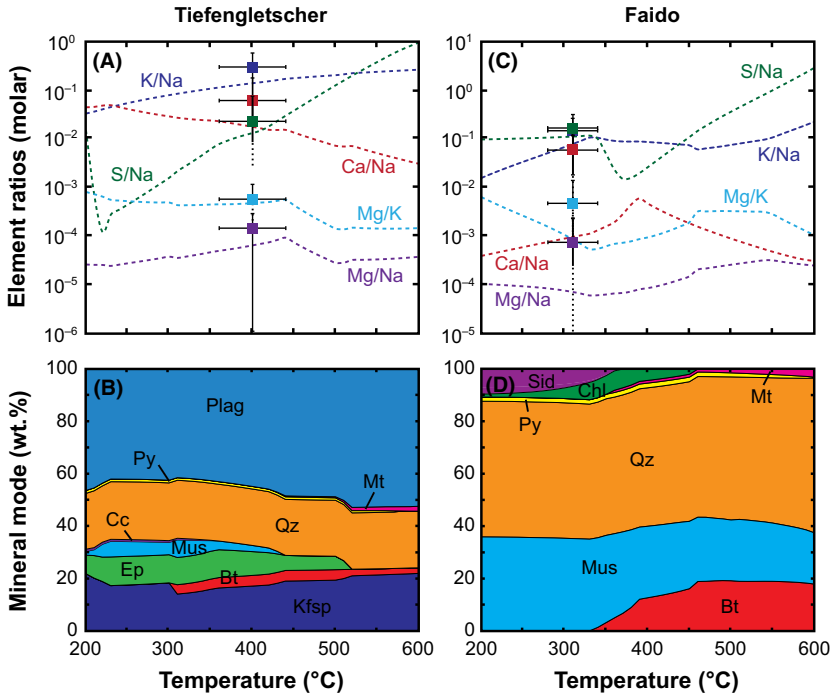

Fig. 12. Comparison between results of fluid–mineral equilibria modeling and analytical data (fluid composition, mineral abundance). Diagrams (A) and (C) show the major element ratios (K/Na, Ca/Na, S/Na, Mg/K and Mg/Na) in the fluid. Dotted lines are calculated element ratios as function of temperature, whereas symbols with error bars are measured values from fluid inclusions (average value for all FIA from one locality). The pressure–temperature conditions for Alpine vein formation were estimated from chemical solute thermometry and fluid inclusion isochores (see text). Diagrams (B) and (D) show predicted mineral abundance as function of temperature, which are in agreement with the mineralogy of the altered host rock in immediate vein contact at the estimated vein formation temperature.

consistently higher in the aqueous–carbonic fluids hosted in amphibolite-facies rocks, compared to the aqueous fluid inclusions in greeschist-facies host rocks. This correlation supports the interpretation that sulfur in the fluid inclusions is produced by prograde metamorphic devolatilization of sulfide-bearing metasediments. Sulfur in metamorphic fluids has been previously reported from Raman spectroscopic studies of fluid inclusions (Dubessy *et al.* 1983) and is thought to be mainly the product of the prograde breakdown of pyrite to pyrrhotite. The metamorphic pyrite to pyrrhotite reaction broadly coincides with the production of water through breakdown of chlorite in mafic sequences near the greenschist–amphibolite-facies transition and the onset of decarbonation reactions in mixed calcite—sheet silicate rocks (Trommsdorff 1966; Powell *et al.* 1991; Craig & Vokes 1993; Phillips & Powell 1993, 2010; Tomkins 2010). The pyrite breakdown reaction has been investigated in graphitic metasedimentary rocks (Frey *et al.* 1980; Ferry 1981; Mohr & Newton 1983; Hall 1986) and metamorphosed massive sulfide deposits (Craig & Vokes 1993; Rosenberg *et al.* 2000; Tomkins 2007). The main conclusion of these studies is that the pyrite breakdown is not strictly an isograd reaction, because it depends not only on the P-T conditions, but also on the bulk composition and oxidation state of the rocks and fluid–mineral mass balance (Hall 1986; Tomkins 2007). This explains why the sulfur concentrations in fluid inclusions of the Alpine fissure veins show only a broad correlation with the metamorphic grade and considerable variation in lithologically different host-rock units that have experienced similar peak metamorphic conditions.

Controls on minor element concentrations in metamorphic fluids

The concentrations of the major rock-forming elements in the fluids that formed the Alpine fissure veins are largely controlled by mineral solubility and fluid–mineral equilibria, as demonstrated by the good agreement

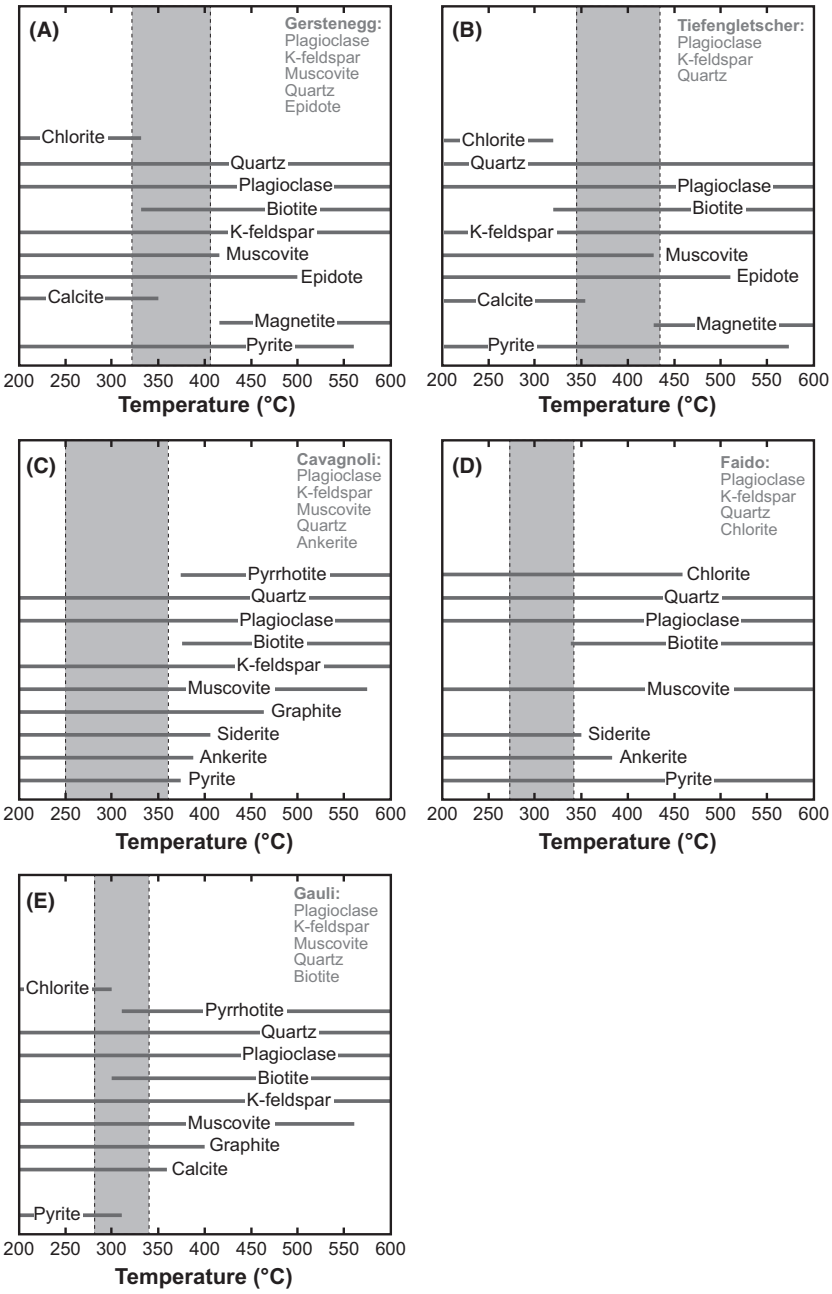

Fig. 13. Diagrams illustrating the predicted host-rock mineralogy as function of temperature, compared to the observed mineral assemblage (list of minerals in the upper right corner of each diagram). The gray fields highlight the temperature range where the modeled mineralogy and mineral composition are in best agreement with the petrographically observed mineralogy. The mineralogy is shown for (A) Gerstenegg, (B) Tiefengletscher, (C) Cavagnoli, (D) Faido, and (E) Gauli.

between modeled and analyzed concentrations. For minor elements such as the ore metals, concentrations in the fluid may be limited by availability in the source rocks, or in host rocks with which the fluids have interacted. Limited availability has been shown for the case of gold, where measured concentrations are lower by one to three orders of magnitude compared to those predicted from solubility calculations (Rauchenstein-Martinek *et al.* 2014). Neither the thermodynamic data for all aqueous species nor the solubility-controlling phases of many trace metals that were analyzed in the fluid inclusions (e.g., Li, Rb, Cs, Sr, Ba, As, and Sb) are accurately known. Therefore, rigorous modeling of their solubility and quantitative analysis of their saturation state cannot be performed at present.

The concentrations of the alkali and alkaline earth metals correlate positively with the salinity (Figs 10 and 11). The fluids found in fissure veins from the Aar massif (Gauli, Gerstenegg, Tiefengletscher) have much higher salinity (up to 10.2 wt.%), which is reflected by much higher concentrations of Na, K, Li, Rb, Cs, Ca, Sr, and Ba compared with the lower-salinity fluids in the Penninic nappes. This trend reflects that alkali and alkaline earth metals are dominantly complexed by chloride

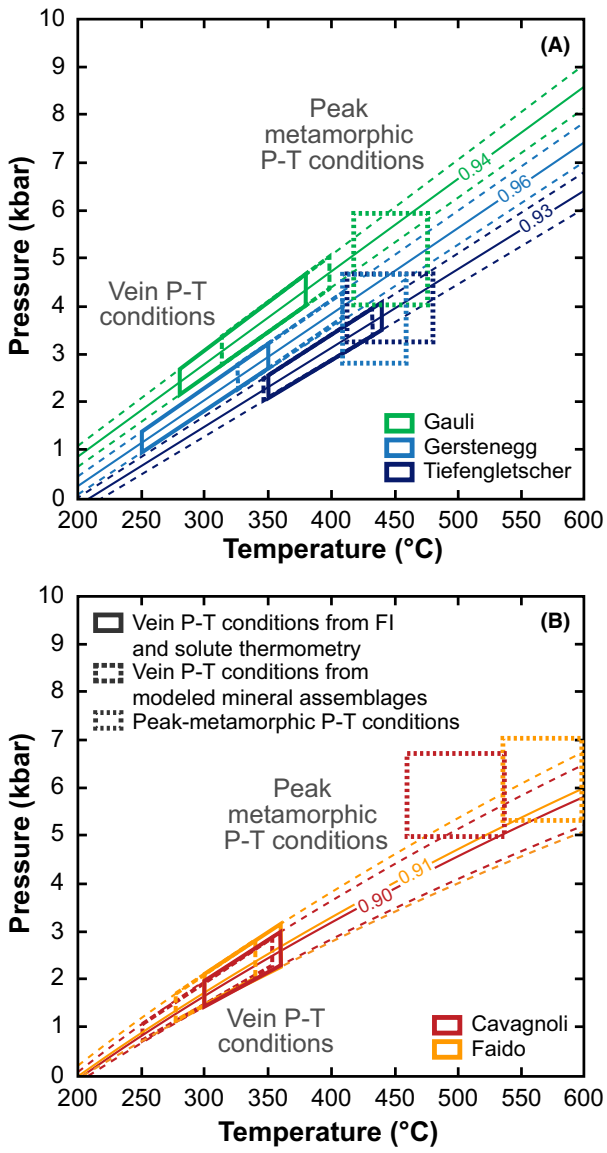

Fig. 14. Diagrams summarizing the estimated pressure-temperature conditions of Alpine fissure vein formation and peak metamorphic conditions of their respective host rocks. The peak metamorphic P-T conditions were adopted from Todd & Engi (1997). The P-T conditions of vein formation were estimated from solute geothermometry, the temperature range of best agreement between modeled and observed mineral assemblages, and fluid inclusion isochores (solid lines: isochores for average fluid density; dashed lines: fluid inclusion isochores for minimum and maximum density based on standard deviations of micothermometric data; numbers on isochores: densities in g cm^{-3}). (A) Summary of pressure–temperature conditions for fissure veins with aqueous (LV) fluid inclusions (Gauli, Gerstenegg, Tiefengletscher). (B) Summary of pressure–temperature conditions for Alpine fissure veins with aqueous–carbonic (LLV) fluid inclusions (Cavagnoli, Faido).

species and that chloride complexes become more stable with increasing temperature (Wood & Samson 1998; Yardley 2005).

Many of the divalent metals such as Fe, Mn, Cu, Zn, and Pb are also dominantly complexed by chloride species (Wood & Samson 1998; Yardley 2005), although the importance of carbonate complexes of Mn and Fe is not fully understood and may be important in aqueous–carbonic fluids (Wolfram & Krupp 1996). Manganese was analyzed in fluid inclusions from all localities and shows a fair correlation with salinity, in agreement with chloride complexation controlling Mn solubility (Suleimenov & Seward 2000; Tian *et al.* 2014). Because of poor elemental detection limits, Fe concentrations are limited to the data from Tiefengletscher (Aar massif) and few data from the other localities. The concentrations of Cu and Pb are positively correlated with those of Zn for the entire dataset (Fig. 11E, G). Solubility control by fluid–mineral equilibria involving Zn and Pb sulfides has been used to explain the clear correlation between the Pb and Zn concentrations in different crustal fluids, and the positive correlations between the concentrations of both metals, salinity, and temperature (Yardley 2005). The observation that the ore metals Cu, Zn, Pb, and Ag have higher concentrations in samples from Tiefengletscher and Faido, compared to Alpine fissure veins that have experienced otherwise identical pressure–temperature conditions, requires an additional explanation. We suggest that host-rock mineralogy, for example the presence or absence of sulfides, may have exerted some control on the base metal concentrations of the fluids in the fissure veins.

Aluminum and titanium behave differently compared with the alkali, alkaline earth and the other divalent metals. The high Al and also Ti concentrations were somewhat unexpected, but the presence of Al minerals (large adularia, albite, and/or muscovite crystals) and Ti minerals (titanite, rutile) in the fissure vein assemblages confirms the mobility of both elements during fluid–rock interaction. The Al concentrations in the fluid inclusions do not correlate with the salinity, but they show a broadly positive correlation with temperature. Measured Al concentrations of 45–89 ppm exceed the predictions from experimental solubility studies and fluid–mineral equilibria modeling (Ragnarsdottir & Walther 1985; Manning 1998, 2006, 2007; Tagirov & Schott 2001; Verlaguet *et al.* 2006; Dolejs & Wagner 2008) by an order of magnitude (Fig. 15). However, comparable Al concentrations in the range of tens of ppm up to more than 100 ppm were previously analyzed in fluid inclusions from orogenic gold quartz veins in the western Alps (Yardley *et al.* 1993), in fluid inclusions from late-metamorphic quartz veins in the Rhenish massif (Marsala *et al.* 2013) and in fluid inclusions from fissure veins hosted by very-low-grade metasediments of the Bündnerschiefer in the Swiss Alps (Miron *et al.* 2013). The solubility and transport of Al in crustal fluids is thought to

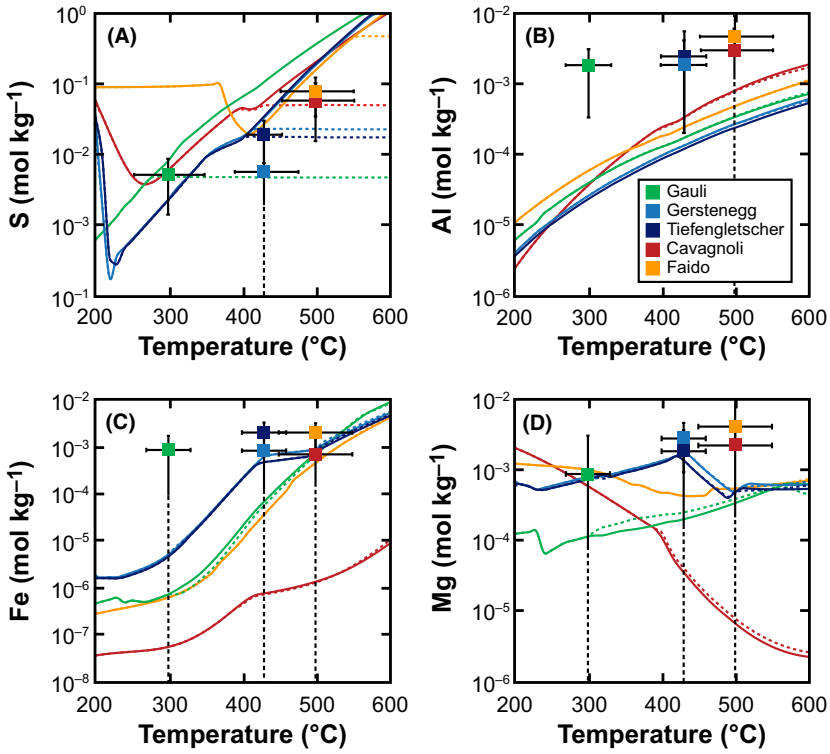

Fig. 15. Comparison between measured (symbols with error bars) and calculated (lines) element concentrations in fluid inclusions from Alpine fissure veins (Gauli, Gerstenegg, Tiefengletscher, Cavagnoli, and Faido). The lines are predicted concentrations as function of temperature. Solid lines represent element solubility calculated by assuming pyrite excess in the rock, while dashed lines were calculated based on measured sulfide concentration in the rock and in the fluid inclusions. The modeling results are in reasonable agreement with the measured fluid inclusion compositions for (A) sulfur, (C) iron, and (D) magnesium, whereas the measured (B) aluminum concentrations are systematically higher than the calculated solubility.

be mainly controlled by Al hydroxy species, whereas complexation with chloride is not considered relevant (Tagirov & Schott 2001). Experimental evidence shows that the Al solubility can be greatly enhanced by one to several orders of magnitude due to the presence of additional ligands such as fluorine, boron, and silica that form stable complexes with Al and that these complexes become more stable at elevated temperatures and pressures (Salvi *et al.* 1998; Tagirov *et al.* 2002a,b, 2004; Manning 2007). Elevated Al concentrations that were found in fluid inclusions from the orogenic gold quartz veins in the southern Alps were related to the formation of stable Al-fluoride complexes (Yardley *et al.* 1993). Fluorine cannot be analyzed by LA-ICPMS and we can therefore not test the effect of fluorine on Al solubility. We tentatively explain the high measured Al concentrations in the fluid inclusions by the combined solubility enhancing effect of Al complexing with fluorine, boron and silica.

Geodynamic framework of Alpine fissure vein formation

Combination of fluid inclusion chemistry, pressure–temperature conditions of vein formation, results from the fluid–mineral equilibria modeling, and published data for peak metamorphic conditions define local segments of the regional pressure–temperature paths of the central Alpine metamorphic dome, as summarized in Fig. 16. Fluid pressures were probably close to the lithostatic load during fissure vein formation, as indicated by structural observations: (1) protracted crystallization of large crystals showing subtle fracturing and overgrowth, but never any collapse and vein re-opening; (2) the mechanical stability of large subhorizontal fissures (Fig. 2A); and (3) the persistence of open en-echelon cavities even in weak host rocks undergoing concurrent ductile deformation (Miron *et al.* 2013). Given the surprisingly constant density and composition of the fluids, despite an apparently protracted dynamic evolution of the fissures, we envision an environment of slow drainage of deeper-sourced metamorphic fluids through a poorly connected fracture network, consistent with the localized occurrence of individual cavities along broadly defined corridors.

Assuming that the fissure veins formed under lithostatic fluid pressure, and taking an average rock density of 2.7 g cm^{-3}, the pressure estimates for the Alpine fissure veins translate into formation depths of 10–17 km depth for Gauli, 8–12 km for Gerstenegg, 8–14 km for Tiefengletscher, 5–11 km for Cavagnoli and 6–10 km for Faido. Figure 16 shows that the fissures formed at similar temperatures between 300 and 430°C. For the locations in the Aar massif, these temperature–depth estimates are broadly consistent with a long-term geothermal gradient of 25°C km^{-1} indicated by zircon fission-track thermochronology (Glotzbach *et al.* 2010)

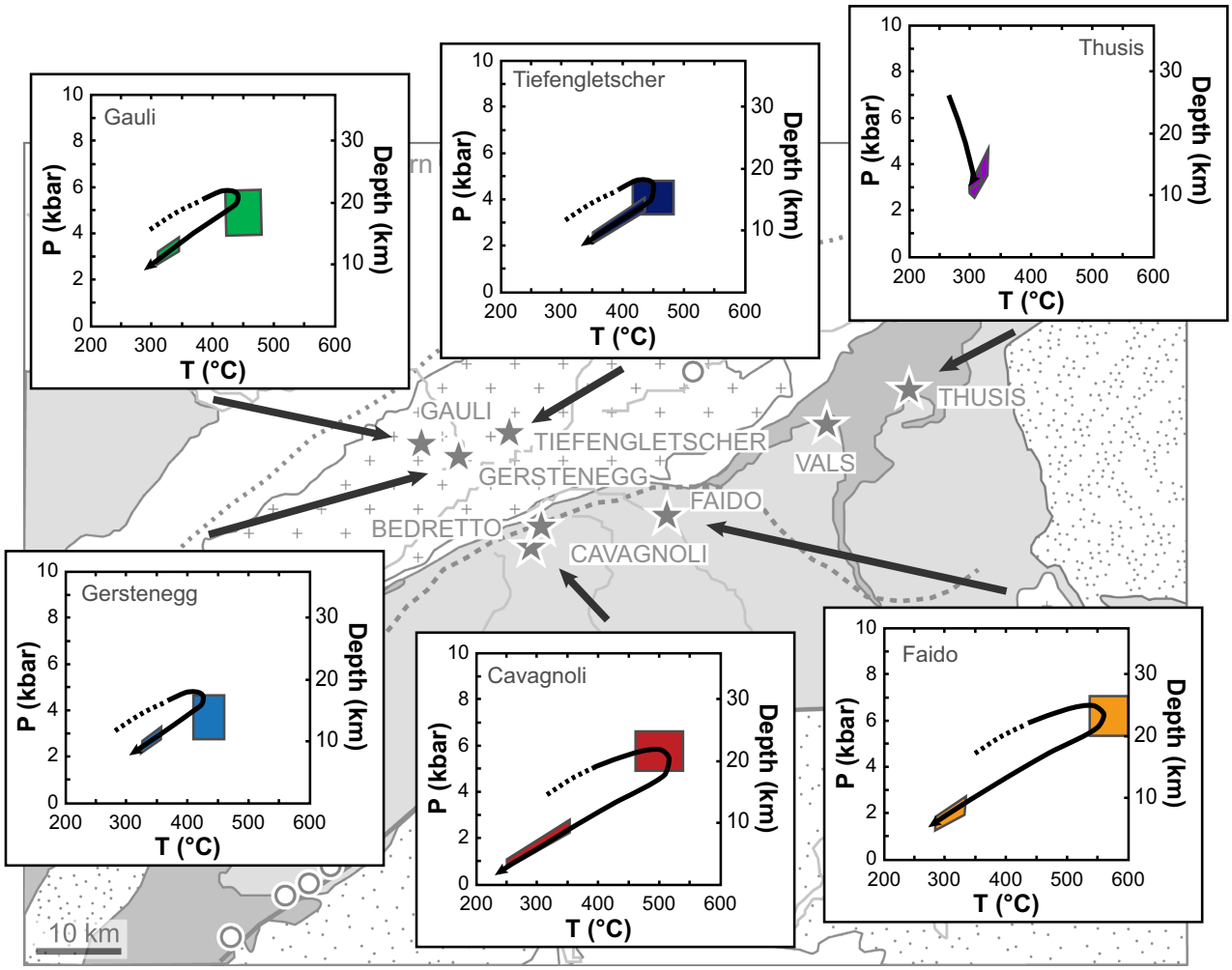

Fig. 16. Geological sketch map of the Central Alps, with superposed pressure–temperature diagrams illustrating the evolution of the fissure veins and their respective host rocks. Colored fields indicate conditions of peak metamorphism and subsequent fissure vein formation, whereas black arrows are interpreted P-T paths. The peak metamorphic pressure–temperature conditions were adopted from Todd & Engi (1997).

and with the small difference between vein-forming and peak metamorphic conditions. For the locations further south, however, deviations between vein-forming conditions and peak metamorphic conditions systematically increase. Apparently, the shallowest veins formed in the southern areas, where peak metamorphic temperatures were highest, that is fissure vein formation is most distinctly retrograde with regard to the local metamorphic P-T path. We cannot exclude postentrapment stretching of the fluid inclusions leading to an underestimation of vein formation pressure, but similar temperatures at shallower depth might be explained by rapid asymmetric uplift of the Lepontine dome after peak metamorphism, centered to the south of our study area (Fig. 1). Fissure veins formed when each location cooled toward the brittle–ductile transition of quartz-rich host rocks, slowly draining fluids from local and subjacent metamorphic rocks as a result of uplift, but prior to erosion and interconnected permeability allowing incursion of meteoric water into texturally distinct epithermal veins (Sharp *et al.* 2005; Diamond & Tarantola 2015).

ACKNOWLEDGEMENTS

This project was funded by the Swiss National Science Foundation (SNF), project No. 200021-130201. We thank A. Willener (KWO) for providing access to the Gerstenegg Alpine fissure vein. T. Good is thanked for preparation of petrographic and fluid inclusion sections and Lydia Zehnder for the XRF analyses of whole-rock samples. The Canton of Ticino (Dipartimento del Territorio and Museo Cantonale di Storia Naturale) is acknowledged for permission of sampling and provision of material from

the Faido tunnel. We are grateful for interesting discussion with Josef Mullis, Larryn Diamond, and Bruce Yardley, and we thank two anonymous Geofluids reviewers for their constructive comments, which helped to improve this manuscript.

REFERENCES

Agard P, Goffé B, Touret JLR, Vidal O (2000) Retrograde mineral and fluid evolution in high-pressure metapelites (Schistes lustrés unit, Western Alps). *Contributions to Mineralogy and Petrology*, **140**, 296–315.

Allan MM, Yardley BWD, Forbes LJ, Shmulovich KI, Banks DA, Shepherd TJ (2005) Validation of LA-ICP-MS fluid inclusion analysis with synthetic fluid inclusions. *American Mineralogist*, **90**, 1767–75.

Arnorsson S (2000) *Isotopic and Chemical Techniques in Geothermal Exploration, Development and Use: Sampling Methods, Data Handling, Interpretation*. International Atomic Energy Agency, Vienna.

Audétat A, Günther D, Heinrich CA (2000) Magmatic-hydrothermal evolution in a fractionating granite: a microchemical study of the Sn-W-F-mineralized Mole Granite (Australia). *Geochimica et Cosmochimica Acta*, **64**, 3373–93.

Bakker RJ (2003) Package FLUIDS 1. Computer programs for analysis of fluid inclusion data and for modelling bulk fluid properties. *Chemical Geology*, **194**, 3–23.

Banks DA, Davies GR, Yardley BWD, McCaig AM, Grant NT (1991) The chemistry of brines from an Alpine thrust system in the central Pyrenees – an application of fluid inclusion analysis to the study of fluid behavior in orogenesis. *Geochimica et Cosmochimica Acta*, **55**, 1021–30.

Baumgartner LP, Ferry JM (1991) A model for coupled fluid-flow and mixed-volatile mineral reactions with applications to regional metamorphism. *Contributions to Mineralogy and Petrology*, **106**, 273–85.

Berger A, Mercolli I, Engi M (2005) The central Lepontine Alps: notes accompanying the tectonic and petrographic map sheet Sopra Ceneri (1:100'000). *Schweizerische Mineralogische und Petrographische Mitteilungen*, **85**, 109–46.

Berger A, Rosenberg C, Schaltegger U (2009) Stability and isotopic dating of monazite and allanite in patially molten rocks: example from the Central Alps. *Swiss Journal of Geosciences*, **102**, 15–29.

Berger A, Schmid SM, Engi M, Bousquet R, Wiederkehr M (2011) Mechanisms of mass and heat transport during Barrovian metamorphism: a discussion based on field evidence from the Central Alps (Switzerland/northern Italy). *Tectonics*, **30**, TC1007.

Bickle MJ, Mckenzie D (1987) The transport of heat and matter by fluids during metamorphism. *Contributions to Mineralogy and Petrology*, **95**, 384–92.

Bodnar RJ (1993) Revised equation and table for determining the freezing-point depression of H_2O-NaCl solutions. *Geochimica et Cosmochimica Acta*, **57**, 683–4.

Boiron MC, Cathelineau M, Banks DA, Fourcade S, Vallance J (2003) Mixing of metamorphic and surficial fluids during the uplift of the Hercynian upper crust: consequences for gold deposition. *Chemical Geology*, **194**, 119–41.

Bousquet R, Oberhänsli R, Goffe B, Jolivet L, Vidal O (1998) High-pressure-low-temperature metamorphism and deformation in the Bündnerschiefer of the Engadine window: implications for the regional evolution of the eastern Central Alps. *Journal of Metamorphic Geology*, **16**, 657–74.

Burke EAJ (2001) Raman microspectrometry of fluid inclusions. *Lithos*, **55**, 139–58.

Burkhard M, Kerrich R (1988) Fluid regimes in the deformation of the Helvetic nappes, Switzerland, as inferred from stable isotope data. *Contributions to Mineralogy and Petrology*, **99**, 416–29.

Burrus RC (1981) Analysis of phase equilibria in C-O-H-S fluid inclusions. *Mineralogical Association of Canada Short Course Series*, **6**, 39–74.

Cartwright I, Buick IS (2000) Fluid generation, vein formation and the degree of fluid–rock interaction during decompression of high-pressure terranes: the Schistes Lustres, Alpine Corsica, France. *Journal of Metamorphic Geology*, **18**, 607–24.

Chi GX, Savard MM (1997) Sources of basinal and Mississippi Valley-type mineralizing brines: mixing of evaporated seawater and halite-dissolution brine. *Chemical Geology*, **143**, 121–5.

Coggon R, Holland TJB (2002) Mixing properties of phengitic micas and revised garnet-phengite thermobarometers. *Journal of Metamorphic Geology*, **20**, 683–96.

Connolly JAD, Thompson AB (1989) Fluid and enthalpy production during regional metamorphism. *Contributions to Mineralogy and Petrology*, **102**, 347–66.

Craig JR, Vokes FM (1993) The metamorphism of pyrite and pyritic ores – an overview. *Mineralogical Magazine*, **57**, 3–18.

Dale J, Powell R, White RW, Elmer FL, Holland TJB (2005) A thermodynamic model for Ca-Na clinoamphiboles in Na_2O-CaO-FeO-MgO-Al_2O_3-SiO_2-H_2O-O for petrological calculations. *Journal of Metamorphic Geology*, **23**, 771–91.

Demartin F, Gramaccioli CM, Pilati T (1994) Paraniite-(Y), a new tungstate arsenate mineral from Alpine fissures. *Schweizerische Mineralogische und Petrographische Mitteilungen*, **74**, 155–60.

Diamond LW (1992) Stability of CO_2 clathrate hydrate+CO_2 liquid+CO_2 vapour+aqueous KCl-NaCl solutions – experimental determination and application to salinity estimates of fluid inclusions. *Geochimica et Cosmochimica Acta*, **56**, 273–80.

Diamond LW, Tarantola A (2015) Interpretation of fluid inclusions in quartz deformed by weak ductile shearing: reconstruction of differential stress magnitudes and pre-deformation fluid properties. *Earth and Planetary Science Letters*, **417**, 107–19.

Dolejs D, Wagner T (2008) Thermodynamic modeling of non-ideal mineral-fluid equilibria in the system Si-Al-Fe-Mg-Ca-Na-K-H-O-Cl at elevated temperatures and pressures: implications for hydrothermal mass transfer in granitic rocks. *Geochimica et Cosmochimica Acta*, **72**, 526–53.

Dubessy J, Geisler D, Kosztolanyi C, Vernet M (1983) The determination of sulfate in fluid inclusions using the mole Raman microprobe – application to a Keuper halite and geochemical consequences. *Geochimica et Cosmochimica Acta*, **47**, 1–10.

Dubessy J, Poty B, Ramboz C (1989) Advances in C-O-H-N-S fluid geochemistry based on micro-Raman spectroscopic analysis of fluid inclusions. *European Journal of Mineralogy*, **1**, 517–34.

Evans KA, Powell R, Holland TJB (2010) Internally consistent data for sulphur-bearing phases and application to the construction of pseudosections for mafic greenschist facies rocks in Na_2O-CaO-K_2O-FeO-MgO-Al_2O_3-SiO_2-CO_2-O-S-H_2O. *Journal of Metamorphic Geology*, **28**, 667–87.

Ferry JM (1981) Petrology of graphitic sulfide-rich schists from south-central Maine – an example of desulfidation during prograde regional metamorphism. *American Mineralogist*, **66**, 908–31.

Ferry JM (1994) A historical review of metamorphic fluid-flow. *Journal of Geophysical Research*, **B99**, 15487–98.

Ferry JM, Dipple GM (1991) Fluid flow, mineral reactions, and metasomatism. *Geology*, **19**, 211–4.

Fournier RO, Truesdell AH (1973) An empirical Na-K-Ca geothermometer for natural waters. *Geochimica et Cosmochimica Acta*, **37**, 1255–75.

Frey M, Ferreiro Mählmann R (1999) Alpine metamorphism of the Central Alps. *Schweizerische Mineralogische und Petrographische Mitteilungen*, **79**, 135–54.

Frey M, Bucher K, Frank E, Mullis J (1980) Alpine metamorphism along the geotraverse Basel-Chiasso: a review. *Eclogae Geologicae Helvetiae*, **73**, 527–46.

Frezzotti ML, Tecce F, Casagli A (2012) Raman spectroscopy for fluid inclusion analysis. *Journal of Geochemical Exploration*, **112**, 1–20.

Frisch W (1979) Tectonic progradation and plate tectonic evolution of the Alps. *Tectonophysics*, **60**, 121–39.

Fusswinkel T, Wagner T, Wälle M, Wenzel T, Heinrich CA, Markl G (2013) Fluid mixing forms basement-hosted Pb-Zn deposits: insight from metal and halogen geochemistry of individual fluid inclusions. *Geology*, **41**, 679–82.

Fyfe WS, Price NJ, Thompson AB (1987) *Fluids in the Earth's Crust*. Elsevier, Amsterdam.

Giggenbach WF (1988) Geothermal solute equilibria – derivation of Na-K-Mg-Ca geoindicators. *Geochimica et Cosmochimica Acta*, **52**, 2749–65.

Glotzbach C, Reinecker J, Danisik M, Rahn M, Frisch W, Spiegel C (2010) Thermal history of the central Gotthard and Aar massifs, European Alps: evidence for steady state, long-term exhumation. *Journal of Geophysical Research-Earth Surface*, **115**, F03017.

Goldfarb RJ, Groves DI (2015) Orogenic gold: common or evolving fluid and metal sources. *Lithos*, **233**, 2–26.

Goldstein RH, Reynolds TJ (1994) Systematics of fluid inclusions in diagenetic minerals. *Society of Sedimentary Geology Short Course Series*, **31**, 1–199.

Groves DI, Goldfarb RJ, Robert F, Hart CJR (2003) Gold deposits in metamorphic belts: overview of current understanding, outstanding problems, future research, and exploration significance. *Economic Geology*, **98**, 1–29.

Grujic D, Mancktelow NS (1996) Structure of the northern Maggia and Lebendun nappes, central Alps, Switzerland. *Eclogae Geologicae Helvetiae*, **89**, 461–504.

Guillong M, Heinrich CA (2007) Sensitivity enhancement in laser ablation ICP-MS using small amounts of hydrogen in the carrier gas. *Journal of Analytical Atomic Spectrometry*, **22**, 1488–94.

Guillong M, Meier DL, Allan MM, Heinrich CA, Yardley BWD (2008) SILLS: a Matlab-based program for the data reduction of laser ablation ICP-MS data of homogeneous materials and inclusions. *Mineralogical Association of Canada Short Course Series*, **40**, 328–33.

Günther D, Frischknecht R, Heinrich CA, Kahlert HJ (1997) Capabilities of an argon fluoride 193 nm excimer laser for laser ablation inductively coupled plasma mass spectrometry microanalysis of geological materials. *Journal of Analytical Atomic Spectrometry*, **12**, 939–44.

Günther D, Audétat A, Frischknecht R, Heinrich CA (1998) Quantitative analysis of major, minor and trace elements in fluid inclusions using laser ablation-inductively coupled plasma mass spectrometry. *Journal of Analytical Atomic Spectrometry*, **13**, 263–70.

Hall AJ (1986) Pyrite-pyrrhotine redox reactions in nature. *Mineralogical Magazine*, **50**, 223–9.

Handy MR, Schmid SM, Bousquet R, Kissling E, Bernoulli D (2010) Reconciling plate-tectonic reconstruction of Alpine Tethys with the geological-geophysical record of spreading and subduction in the Alps. *Earth Science Reviews*, **102**, 121–58.

Heijlen W, Banks DA, Muchez P, Stensgard BM, Yardley BWD (2008) The nature of mineralizing fluids of the Kipushi Zn-Cu deposit, Katanga, Democratic Repubic of Congo: quantitative fluid inclusion analysis using laser ablation ICP-MS and bulk crush-leach methods. *Economic Geology*, **103**, 1459–82.

Heinrich CA (1986) Eclogite facies regional metamorphism of hydrous mafic rocks in the Central Alpine Adula nappe. *Journal of Petrology*, **27**, 123–54.

Heinrich CA, Ryan CG, Mernagh TP, Eadington PJ (1992) Segregation of ore metals between magmatic brine and vapor: a fluid inclusion study using PIXE microanalysis. *Economic Geology*, **87**, 1566–83.

Heinrich CA, Bain JHC, Fardy JJ, Waring CL (1993) Br/Cl geochemistry of hydrothermal brines associated with Proterozoic metasediment-hosted copper mineralization at Mount Isa, northern Australia. *Geochimica et Cosmochimica Acta*, **57**, 2991–3000.

Heinrich CA, Pettke T, Halter WE, Aigner-Torres M, Audetat A, Günther D, Hattendorf B, Bleiner D, Guillong M, Horn I (2003) Quantitative multi-element analysis of minerals, fluid and melt inclusions by laser-ablation inductively-coupled-plasma mass-spectrometry. *Geochimica et Cosmochimica Acta*, **67**, 3473–97.

Helgeson HC, Kirkham DH, Flowers GC (1981) Theoretical prediction of the thermodynamic behavior of aqueous electrolytes at high pressures and temperatures. IV. Calculation of activity coefficients, osmotic coefficients, and apparent molal and standard and relative partial molal properties to 600°C and 5 KB. *American Journal of Science*, **281**, 1249–516.

Hofmann BA, Knill MD (1996) Geochemistry and genesis of the Lengenbach Pb-Zn-As-Tl-Ba-mineralization, Binn valley, Switzerland. *Mineralium Deposita*, **31**, 319–39.

Holland T, Powell R (1996) Thermodynamics of order-disorder in minerals. II. Symmetric formalism applied to solid solutions. *American Mineralogist*, **81**, 1425–37.

Holland TJB, Powell R (1998) An internally consistent thermodynamic data set for phases of petrological interest. *Journal of Metamorphic Geology*, **16**, 309–43.

Holland T, Powell R (2003) Activity-composition relations for phases in petrological calculations: an asymmetric multicomponent formulation. *Contributions to Mineralogy and Petrology*, **145**, 492–501.

Holland T, Baker J, Powell R (1998) Mixing properties and activity-composition relationships of chlorites in the system MgO-FeO-Al_2O_3-SiO_2-H_2O. *European Journal of Mineralogy*, **10**, 395–406.

Hollister LS, Burrus RC (1976) Phase equilibria in fluid inclusions from the Khtada Lake metamorphic complex. *Geochimica et Cosmochimica Acta*, **40**, 163–75.

Hsü KJ (1991) Exhumation of high-pressure metamorphic rocks. *Geology*, **19**, 107–10.

Hunziker JC, Desmons J, Martinotti G (1989) Alpine thermal evolution of the Western Alps: a review. *Memoir Societa Geologia Italia*, **29**, 43–56.

Hurford AJ (1986) Cooling and uplift patterns in the Lepontine Alps South Central Switzerland and an age of vertical movement of the Insubric fault line. *Contributions to Mineralogy and Petrology*, **92**, 413–27.

Indergand-Helfenstein P (2005) Historische Kristallfunde im Kanton Uri. *Historischer Verein Uri Historisches Neujahrsblatt Neue Folge*, **60**, 57–79.

Janots E, Engi M, Rubatto D, Berger A, Gregory C, Rahn M (2009) Metamorphic rates in collisional orogeny from in situ allanite and monazite dating. *Geology*, **37**, 11–4.

Janots E, Berger A, Gnos E, Whitehouse M, Lewin E, Pettke T (2012) Constraints on fluid evolution during metamorphism from U-Th-Pb systematics in Alpine hydrothermal monazite. *Chemical Geology*, **326**, 61–71.

Johnson WM, Maxwell JA (1981) *Rock and Mineral Analysis*. 2nd edn. Wiley, New York.

Johnson JW, Oelkers EH, Helgeson HC (1992) SUPCRT92: a software package for calculating the standard molal thermodynamic properties of minerals, gases, aqueous species, and reactions from 1 to 5000 bar and 0 to 1000°C. *Computers & Geosciences*, **18**, 899–947.

Karpov IK, Chudnenko KV, Kulik DA (1997) Modeling chemical mass transfer in geochemical processes: thermodynamic relations, conditions of equilibria, and numerical algorithms. *American Journal of Science*, **297**, 767–806.

Kendrick MA, Phillips D, Wallace M, Miller JML (2011) Halogens and noble gases in sedimentary formation waters and Zn-Pb deposits: a case study from the Lennard Shelf, Australia. *Applied Geochemistry*, **26**, 2089–100.

Kharaka YK, Mariner RH (1989) Chemical geothermometers and their application to formation waters from sedimentary basins. In: *Thermal History of Sedimentary Basins* (eds Naeser ND, McCulloh TH), pp. 99–117. Springer, New York.

Kharaka YK, Lico MS, Law LM (1982) Chemical geothermometers applied to formation waters, Gulf-of-Mexico and California basins. *American Association of Petroleum Geologists Bulletin*, **66**, 588.

Kulik DA, Wagner T, Dmytrieva SV, Kosakowski G, Hingerl FF, Chudnenko KV, Berner UR (2013) GEM-Selektor geochemical modeling package: revised algorithm and GEMS3K numerical kernel for coupled simulation codes. *Computational Geosciences*, **17**, 1–24.

Manning CE (1998) Fluid composition at the blueschist – eclogite transition in the model system Na_2O-MgO-Al_2O_3-SiO_2-H_2O-HCl. *Schweizerische Mineralogische und Petrographische Mitteilungen*, **78**, 225–42.

Manning CE (2006) Mobilizing aluminum in crustal and mantle fluids. *Journal of Geochemical Exploration*, **89**, 251–3.

Manning CA (2007) Solubility of corundum plus kyanite in H_2O at 700°C and 10 kbar: evidence for Al-Si complexing at high pressure and temperature. *Geofluids*, **7**, 258–69.

Marquer D, Burkhard M (1992) Fluid circulation, progressive deformation and mass-transfer in the upper crust: the example of basement-cover relationships in the External Crystalline Massifs, Switzerland. *Journal of Structural Geology*, **14**, 1047–57.

Marsala A, Wagner T, Wälle M (2013) Late-metamorphic veins record deep ingression of meteoric water: a LA-ICPMS fluid inclusion study from the fold-and-thrust belt of the Rhenish Massif, Germany. *Chemical Geology*, **351**, 134–53.

McCaffrey MA, Lazar B, Holland HD (1987) The evaporation path of seawater and the coprecipitation of Br^- and K^+ with halite. *Journal of Sedimentary Petrology*, **57**, 928–37.

McCaig AM, Tritlla J, Banks DA (2000) Fluid mixing and recycling during Pyrenean thrusting: evidence from fluid inclusion halogen ratios. *Geochimica et Cosmochimica Acta*, **64**, 3395–412.

Meere PA, Banks DA (1997) Upper crustal fluid migration: an example from the Variscides of SW Ireland. *Journal of the Geological Society London*, **154**, 975–85.

Menzies CD, Teagle DAH, Craw D, Cox SC, Boyce AJ, Barrie CD, Roberts S (2014) Incursion of meteoric waters into the ductile regime in an active orogen. *Earth and Planetary Science Letters*, **399**, 1–13.

Mercolli I, Schenker F, Stalder HA (1984) Geochemie der Veränderungen von Granit durch hydrothermale Lösungen (Zentr. Aaregranit). *Schweizerische Mineralogische und Petrographische Mitteilungen*, **64**, 67–88.

Miron GD, Wagner T, Wälle M, Heinrich CA (2013) Major and trace-element composition and pressure-temperature evolution of rock-buffered fluids in low-grade accretionary-wedge metasediments, Central Alps. *Contributions to Mineralogy and Petrology*, **165**, 981–1008.

Mohr DW, Newton RC (1983) Kyanite-staurolite metamorphism in sulfidic schists of the Anakeesta Formation, Great Smoky Mountains, North-Carolina. *American Journal of Science*, **283**, 97–134.

Mullis J (1975) Growth conditions of quartz crystals from Val d'Illiez (Valais, Switzerland). *Schweizerische Mineralogische und Petrographische Mitteilungen*, **55**, 419–29.

Mullis J (1987) Fluid inclusion studies during very low-grade metamorphism. In: *Low Temperature Metamorphism* (ed Frey M), pp. 162–99. Blackwell, Glasgow.

Mullis J (1988) Rapid subsidence and upthrusting in the Northern Apennines, deduced by fluid inclusion studies in quartz crystals from Porretta Terme. *Schweizerische Mineralogische und Petrographische Mitteilungen*, **88**, 157–70.

Mullis J (1996) P-T-t path of quartz formation in extensional veins of the Central Alps. *Schweizerische Mineralogische und Petrographische Mitteilungen*, **76**, 159–64.

Mullis J, Dubessy J, Poty B, O'Neil J (1994) Fluid regimes during late stages of a continental collision – physical, chemical, and stable-isotope measurements of fluid inclusions in fissure quartz from a geotraverse through the Central Alps, Switzerland. *Geochimica et Cosmochimica Acta*, **58**, 2239–67.

Mullis J, Vennemann T, O'Neil JR (2001) Deep percolating meteoric waters in the Central Alps. *Journal of Conference Abstracts*, **6**, 279.

Nieva D, Nieva R (1987) Developments in geothermal energy in Mexico – part twelve. A cationic geothermometer for prospecting of geothermal resources. *Heat Recovery Systems and CHP*, **7**, 243–58.

Niggli E (1970) Alpine Metamorphose und alpine Gebirgsbildung. *Fortschritte der Mineralogie*, **47**, 16–26.

Niggli E, Niggli KR (1965) Karten der Verbreitung einiger Mineralien der alpidischen Metamorphose in den Schweizer Alpen (Stilpnomelan, Alkali-Amphibol, Chloritoid, Staurolith, Disthen, Sillimanit). *Schweizerische Mineralogische und Petrographische Mitteilungen*, **58**, 335–68.

Norris RJ, Henley RW (1976) Dewatering of a metamorphic pile. *Geology*, **80**, 333–6.

Oberhänsli R, Goffé B, Bousquet R (1995) Record of a HP-LT metamorphic evolution in the Valais zone: geodynamic implications. *Bolletino del Museo Regionale di Scienze Naturali*, **13**, 221–40.

Oliver NHS (1996) Review and classification of structural controls on fluid flow during regionel metamorphism. *Journal of Metamorphic Geology*, **14**, 477–92.

Oliver NHS, Bons PD (2001) Mechanisms of fluid flow and fluid–rock interaction in fossil metamorphic hydrothermal systems inferred from vein–wallrock patterns, geometry and microstructure. *Geofluids*, **1**, 137–62.

Pfiffner OA, Ellis S, Beaumont C (2000) Collision tectonics in the Swiss Alps: insight from geodynamic modeling. *Tectonics*, **19**, 1065–94.

Phillips GN, Powell R (1993) Link between gold provinces. *Economic Geology*, **88**, 1084–98.

Phillips GN, Powell R (2010) Formation of gold deposits: a metamorphic devolatilization model. *Journal of Metamorphic Geology*, **28**, 689–718.

Poty B, Stalder HA, Weisbrod AM (1974) Fluid inclusion studies in quartz from fissures of Western and Central Alps. *Schweizerische Mineralogische und Petrographische Mitteilungen*, **54**, 717–52.

Powell R, Holland T (1993) On the formulation of simple mixing models for complex phases. *American Mineralogist*, **78**, 1174–80.

Powell R, Holland T (1999) Relating formulations of the thermodynamics of mineral solid solutions: activity modeling of pyroxenes, amphiboles, and micas. *American Mineralogist*, **84**, 1–14.

Powell R, Will TM, Phillips GN (1991) Metamorphism in Archean greenstone belts – calculated fluid compositions and implications for gold mineralization. *Journal of Metamorphic Geology*, **9**, 141–50.

Purdy JW, Stalder HA (1973) K-Ar ages of fissure minerals from the Swiss Alps. *Schweizerische Mineralogische und Petrographische Mitteilungen*, **53**, 79–98.

Ragnarsdottir KV, Walther JV (1985) Experimental determination of corundum solubilities in pure water between 400-700°C and 1-3 kbar. *Geochimica et Cosmochimica Acta*, **49**, 2109–15.

Rauchenstein-Martinek K, Wagner T, Wälle M, Heinrich CA (2014) Gold concentrations in metamorphic fluids: a LA-ICPMS fluid inclusion study from the Alpine orogenic belt. *Chemical Geology*, **385**, 70–83.

Ridley JR (1993) The relations between mean rock stress and fluid flow in the crust: with reference to vein-and lode-style gold deposits. *Ore Geology Reviews*, **8**, 23–37.

Ridley JR, Diamond LW (2000) Fluid chemistry of orogenic lode-gold deposits and implications for genetic models. *Reviews in Economic Geology*, **13**, 141–62.

Rosenberg JL, Spry PG, Jacobson CE, Vokes FM (2000) The effects of sulfidation and oxidation during metamorphism on compositionally varied rocks adjacent to the Bleikvassli Zn-Pb-(Cu) deposit, Nordland, Norway. *Mineralium Deposita*, **35**, 714–26.

Rubatto D, Hermann J, Berger A, Engi M (2009) Protracted fluid-induced melting during Barrovian metamorphism in the Central Alps. *Contributions to Mineralogy and Petrology*, **158**, 703–22.

Rudnick RL, Gao S (2004) Composition of the continental crust. *Treatise on Geochemistry*, **3**, 1–64.

Salvi S, Pokrovski GS, Schott J (1998) Experimental investigation of aluminum-silica aqueous complexing at 300°C. *Chemical Geology*, **151**, 51–67.

Schlunegger F, Willett S (1999) Spatial and temporal variations in exhumation in the Central Swiss Alps and implications for exhumation mechanisms. *Geological Society Special Publications*, **154**, 157–79.

Schmid SM, Pfiffner OA, Froitzheim N, Schönborn G, Kissling E (1996) Geophysical-geological transect and tectonic evolution of the Swiss-Italian Alps. *Tectonics*, **15**, 1036–64.

Schmid SM, Fügenschuh B, Kissling E, Schuster R (2004) Tectonic map and overall architecture of the Alpine orogen. *Eclogae Geologicae Helvetiae*, **97**, 93–117.

Seo JH, Guillong M, Aerts M, Zajacz Z, Heinrich CA (2011) Microanalysis of S, Cl, and Br in fluid inclusions by LA-ICP-MS. *Chemical Geology*, **284**, 35–44.

Sharp ZD, Masson H, Lucchini R (2005) Stable isotope geochemistry and formation mechanisms of quartz veins. Extreme paleoaltitudes of the Central Alps in the Neogene. *American Journal of Science*, **305**, 187–219.

Shock EL, Helgeson HC (1988) Calculation of the thermodynamic and transport properties of aqueous species at high pressures and temperatures: correlation algorithms for ionic species and equation of state predictions to 5 kb and 1000°C. *Geochimica et Cosmochimica Acta*, **52**, 2009–36.

Shock EL, Helgeson HC, Sverjensky DA (1989) Calculation of the thermodynamic and transport properties of aqueous species at high pressures and temperatures: standard partial molal properties of inorganic neutral species. *Geochimica et Cosmochimica Acta*, **53**, 2157–83.

Shock EL, Sassani DC, Willis M, Sverjensky DA (1997) Inorganic species in geological fluids: correlations among standard molal thermodynamic properties of aqueous ions and hydroxide complexes. *Geochimica et Cosmochimica Acta*, **61**, 907–50.

Spycher N, Peiffer L, Sonnenthal EL, Saldi G, Reed MH, Kennedy BM (2014) Integrated multicomponent solute geothermometry. *Geothermics*, **51**, 113–23.

Stalder HA (1964) Petrographische und mineralogische Untersuchungen im Grimselgebiet. *Schweizerische Mineralogische und Petrographische Mitteilungen*, **44**, 187–398.

Stalder HA (1986) Beschreibung der geschützten Mineralkluft Gerstenegg, Grimsel, Bern. *Mitteilungen der Naturforschenden Gesellschaft Bern*, **43**, 41–60.

Stalder HA, De Quervain F, Niggli P, Graeser S (1973) *Die Mineralfunde der Schweiz*. Wepf Publisher, Basel, 433 pp.

Stober I, Bucher K (1999) Origin of salinity of deep groundwater in crystalline rocks. *Terra Nova*, **11**, 181–5.

Stoffell B, Appold MS, Wilkinson JJ, McClean NA, Jeffries TE (2008) Geochemistry and evolution of Mississippi Valley-Type mineralizing brines from the Tri-State and northern Arkansas districts determined by LA-ICP-MS microanalysis of fluid inclusions. *Economic Geology*, **103**, 1411–35.

Suleimenov OM, Seward TM (2000) Spectrophotometric measurements of metal complex formation at high temperatures: the stability of Mn(II) chloride species. *Chemical Geology*, **167**, 177–92.

Sverjensky DA, Shock EL, Helgeson HC (1997) Prediction of the thermodynamic properties of aqueous metal complexes to 1000°C and 5 kb. *Geochimica et Cosmochimica Acta*, **61**, 1359–412.

Tagirov B, Schott J (2001) Aluminum speciation in crustal fluids revisited. *Geochimica et Cosmochimica Acta*, **65**, 3965–92.

Tagirov B, Zotov AV, Akinfiev NN (1997) Experimental study of dissociation of HCl from 350 to 500°C and from 500 to 2500 bars. Thermodynamic properties of HCl^0(aq). *Geochimica et Cosmochimica Acta*, **61**, 4267–80.

Tagirov B, Schott J, Harrichourry JC, Salvi S (2002a) Experimental study of aluminum speciation in fluoride-rich supercritical fluids. *Geochimica et Cosmochimica Acta*, **66**, 2013–24.

Tagirov B, Schott J, Harrichoury JC (2002b) Experimental study of aluminum-fluoride complexation in near-neutral and alkaline solutions to 300°C. *Chemical Geology*, **184**, 301–10.

Tagirov B, Schott J, Harrichoury JC, Escalier J (2004) Experimental study of the stability of aluminate-borate complexes in hydrothermal solutions. *Geochimica et Cosmochimica Acta*, **68**, 1333–45.

Tarantola A, Mullis J, Vennemann T, Dubessy J, de Capitani C (2007) Oxidation of methane at the CH_4/H_2O-(CO_2) transition zone in the external part of the Central Alps, Switzerland: evidence from stable isotope investigations. *Chemical Geology*, **237**, 329–57.

Tarantola A, Mullis J, Guillaume D, Dubessy J, de Capitani C, Abdelmoula M (2009) Oxidation of CH_4 to CO_2 and H_2O by chloritization of detrital biotite at 270 ± 5°C in the external part of the Central Alps, Switzerland. *Lithos*, **112**, 497–510.

Templeton AS, Chamberlain CP, Koons PO, Craw D (1999) Stable isotopic evidence for mixing between metamorphic fluids and surface-derived waters during recent uplift of the Southern Alps, New Zealand. *Earth and Planetary Science Letters*, **154**, 73–92.

Thébaud N, Philippot P, Rey P, Cauzid J (2006) Composition and origin of fluids associated with lode gold deposits in a Mesoarchean greenstone belt (Warrawoona Syncline, Pilbara Craton, Western Australia) using synchrotron radiation X-ray fluorescence. *Contributions to Mineralogy and Petrology*, **152**, 485–503.

Thiery R, van den Kerkhof AM, Dubessy J (1994) vX properties of CH_4-CO_2 and CO_2-N_2 fluid inclusions; modelling for T < 31°C and P < 400 bars. *European Journal of Mineralogy*, **6**, 753–71.

Tian Y, Etschmann B, Mei Y, Grundler PV, Testemale D, Hazeman JL, Elliott P, Ngothai Y, Brugger J (2014) Speciation and thermodynamic properties of manganese(II) chloride complexes in hydrothermal fluids: in situ XAS study. *Geochimica et Cosmochimica Acta*, **129**, 77–95.

Todd CS, Engi M (1997) Metamorphic field gradients in the Central Alps. *Journal of Metamorphic Geology*, **15**, 513–30.

Tomkins AG (2007) Three mechanisms of ore re-mobilisation during amphibolite facies metamorphism at the Montauban Zn-Pb-Au-Ag deposit. *Mineralium Deposita*, **42**, 627–37.

Tomkins AG (2010) Windows of metamorphic sulfur liberation in the crust: implications for gold deposit genesis. *Geochimica et Cosmochimica Acta*, **74**, 3246–59.

Touret J (1982) An empirical phase diagram for a part of the N_2-CO_2 system at low temperature. *Chemical Geology*, **37**, 49–58.

Touret JLR (2001) Fluids in metamorphic rocks. *Lithos*, **55**, 1–25.

Tricart P (1984) From passive margin to continental collision: a tectonic scenario for the Western Alps. *American Journal of Science*, **284**, 97–120.

Trommsdorff V (1966) Progressive Metamorphose kieseliger Karbonatgesteine in den Zentralalpen zwischen Bernina und Simplon. *Schweizerische Mineralogische und Petrographische Mitteilungen*, **46**, 431–60.

Trümpy R (1960) Paleotectonic evolution of the Central and Western Alps. *Geological Society of America Bulletin*, **71**, 843–928.

Verlaguet A, Brunet F, Goffe B, Murphy WM (2006) Experimental study and modeling of fluid reaction paths in the quartz-kyanite ± muscovite-water system at 0.7 GPa in the 350-550°C range: implications for Al selective transfer during metamorphism. *Geochimica et Cosmochimica Acta*, **70**, 1772–88.

Vialon P (1990) Deep Alpine structures and geodynamic evolution: an introduction and outline of a new interpretation. *Memoirs Societe Geologique France*, **156**, 7–14.

Wagner T, Kulik DA, Hingerl FF, Dmytrieva SV (2012) GEM-Selektor geochemical modeling package: TSolMod library and data interface for multicomponent phase models. *Canadian Mineralogist*, **50**, 1173–95.

Walther JV (1997) Determination of activity coefficients of neutral species in supercritical H_2O solutions. *Geochimica et Cosmochimica Acta*, **61**, 3311–8.

Walther JV (2001) Experimental determination and analysis of the solubility of corundum in 0.1 and 0.5 m NaCl solutions between 400 and 600°C from 0.5 to 2.0 kbar. *Geochimica et Cosmochimica Acta*, **65**, 2843–51.

Wei CJ, Powell R, Zhang LF (2003) Eclogites from the south Tianshan, NW China: petrological characteristics and calculated mineral equilibria in the Na_2O-CaO-FeO-MgO-Al_2O_3-SiO_2-H_2O system. *Journal of Metamorphic Geology*, **21**, 163–79.

Weisenberger T, Bucher K (2010) Zeolites in fissures of granites and gneisses of the Central Alps. *Journal of Metamorphic Geology*, **28**, 825–47.

Wenk E (1970) Zur Regionalmetamorphose und Ultrametamorphose im Lepontin. *Fortschritte der Mineralogie*, **47**, 34–51.

Wickham SM, Taylor HP (1985) Stable isotopic evidence for large-scale seawater infiltration in a regional metamorphic terrane; the Trois Seigneurs Massif, Pyrenees, France. *Contributions to Mineralogy and Petrology*, **91**, 122–37.

Wiederkehr M, Sudo M, Bousquet R, Berger A, Schmid SM (2009) Alpine orogenic evolution from subduction to collisional thermal overprint: the $^{40}Ar/^{39}Ar$ age constraints from the Valaisan Ocean, central Alps. *Tectonics*, **28**, TC6009.

Wiederkehr M, Bousquet R, Ziemann MA, Berger A, Schmid SM (2011) 3-D assessment of peak-metamorphic conditions by Raman spectroscopy of carbonaceous material: an example from the margin of the Lepontine dome (Swiss Central Alps). *International Journal of Earth Sciences*, **100**, 1029–63.

Wilson AD (1960) The micro-determination of ferrous iron in silicate minerals by a volumetric and a colorimetric method. *Analyst*, **85**, 823–7.

Wolfram O, Krupp RE (1996) Hydrothermal solubility of rhodochrosite, Mn(II) speciation, and equilibrium constants. *Geochimica et Cosmochimica Acta*, **60**, 3983–94.

Wood SA, Samson IM (1998) Solubility of ore minerals and complexation of ore minerals in hydrothermal solutions. *Reviews in Economic Geology*, **10**, 33–80.

Wülser PA, Brugger J, Foden J, Pfeifer HR (2011) The sandstone-hosted Beverley uranium Deposit, Lake Frome Basin, South Australia: mineralogy, geochemistry, and a time-constrained model for its genesis. *Economic Geology*, **106**, 835–67.

Yardley BWD (1983) Quartz veins and devolatilization during metamorphism. *Journal of the Geological Society London*, **140**, 657–63.

Yardley BWD (2005) Metal concentrations in crustal fluids and their relationship to ore formation. *Economic Geology*, **100**, 613–32.

Yardley BWD (2013) The chemical composition of metasomatic fluids in the crust. In: *Metasomatism and the Chemical Transformation of Rocks* (eds Harlov DE, Austrheim H), pp. 17–51. Springer, Heidelberg.

Yardley BWD, Banks DA, Bottrell SH, Diamond LW (1993) Post-metamorphic gold quartz veins from NW Italy – the composition and origin of the ore Fluid. *Mineralogical Magazine*, **57**, 407–22.

Zhang Y, Frantz JD (1987) Determination of homogenization temperature and densities of supercritical fluid in the system NaCl-KCl-$CaCl_2$-H_2O using synthetic fluid inclusions. *Chemical Geology*, **64**, 335–50.

SUPPORTING INFORMATION

Additional Supporting Information may be found online in the supporting information tab for this article:

Data S1. Fluid inclusion data (Thusis, Gauli, Gerstenegg, Tiefengletscher, Vals, Bedretto, Cavagnoli, and Faido).

GEOFLUIDS

Volume 16, Number 5, December 2016

ISSN 1468-8115

CONTENTS

WILEY
Blackwell

Geofluids **is abstracted/indexed in** ***Chemical Abstracts***

This journal is available online at Wiley Online Library.
Visit onlinelibrary.wiley.com to search the articles and register for table of contents and e-mail alerts.